

Reduced-order models for microelectromechanical rectangular and circular plates incorporating the Casimir force

R.C. Batra^{a,*}, M. Porfiri^b, D. Spinello^c

^a Department of Engineering Science & Mechanics, Virginia Polytechnic Institute & State University, Blacksburg, VA 24061, USA

^b Department of Mechanical and Aerospace Engineering, Polytechnic University, Brooklyn, NY 11201, USA

^c The Bradley Department of Electrical & Computer Engineering, Virginia Polytechnic Institute & State University, Blacksburg, VA 24061, USA

Received 29 May 2007; received in revised form 16 February 2008

Available online 29 February 2008

Abstract

We consider the von Kármán nonlinearity and the Casimir force to develop reduced-order models for prestressed clamped rectangular and circular electrostatically actuated microplates. Reduced-order models are derived by taking flexural vibration mode shapes as basis functions for the transverse displacement. The in-plane displacement vector is decomposed as the sum of displacements for irrotational and isochoric waves in a two-dimensional medium. Each of these two displacement vector fields satisfies an eigenvalue problem analogous to that of transverse vibrations of a linear elastic membrane. Basis functions for the transverse and the in-plane displacements are related by using the nonlinear equation governing the plate in-plane motion. The reduced-order model is derived from the equation yielding the transverse deflection of a point. For static deformations of a plate, the pull-in parameters are found by using the displacement iteration pull-in extraction method. Reduced-order models are also used to study linear vibrations about a predeformed configuration. It is found that 9 basis functions for a rectangular plate give a converged solution, while 3 basis functions give pull-in parameters with an error of at most 4%. For a circular plate, 3 basis functions give a converged solution while the pull-in parameters computed with 2 basis functions have an error of at most 3%. The value of the Casimir force at the onset of pull-in instability is used to compute device size that can be safely fabricated.

© 2008 Elsevier Ltd. All rights reserved.

Keywords: von Kármán nonlinearity; Reduced-order nonlinear models; Frequencies; Clamped microelectromechanical plates; Casimir force

1. Introduction

Electrostatically actuated microelectromechanical systems (MEMS) are being used as transistors, switches, micro-mirrors, pressure sensors, micro-pumps, moving valves, and micro-grippers, see for example [Nguyen et al. \(1998\)](#), [Hung and Senturia \(1999\)](#), [Gupta et al. \(1997\)](#), [Chu et al. \(1996\)](#). An electrostatically actuated MEMS is comprised of a conductive deformable body suspended above a rigid grounded body ([Pelesko](#)

* Corresponding author. Tel.: +1 540 231 6051.

E-mail addresses: rbatra@vt.edu (R.C. Batra), mporfiri@poly.edu (M. Porfiri), dspinell@vt.edu (D. Spinello).

and Bernstein, 2002). An applied direct current (DC) voltage between the two bodies results in the deflection of the deformable body, and a consequent change in the system capacitance. When an alternating current (AC) is superimposed on the DC voltage to excite harmonic motions of the system, resonant devices are obtained. These devices are used in signal filtering, and chemical and mass sensing, see for example Abdel-Rahman et al. (2002), Nayfeh and Younis (2005), Rhoads et al. (2006), Tilmans and Legtenberg (1994b), Younis and Nayfeh (2003), Krylov and Maimon (2004), Kuang and Chen (2004), Xie et al. (2003).

The applied DC voltage has an upper limit, beyond which the electrostatic force is not balanced by the elastic restoring force in the deformable conductor. Beyond this critical voltage, the deformable conductor snaps and touches the lower rigid plate, and the MEMS eventually collapses. This phenomenon, called pull-in instability, has been first observed experimentally by Taylor (1968), Nathanson et al. (1967). The critical displacement and the critical voltage associated with this instability are called pull-in displacement and pull-in voltage, respectively. Their accurate evaluation is crucial in the design of electrostatically actuated MEMS. In particular, in micro-mirrors (Hung and Senturia, 1999) and micro-resonators (Tilmans and Legtenberg, 1994a) the designer avoids this instability in order to achieve stable motions; while in switching applications (Nguyen et al., 1998) the designer exploits this effect to optimize the performance of the device.

For a wide class of electrostatic MEMS, the deformable electrode is initially a flat body whose thickness h is much smaller than its characteristic in-plane dimension ℓ , see, Pelesko and Triolo (2001). Such electrodes can be regarded as 2D plate-like bodies. Since $h/\ell \ll 1$, an approximate distributed model can be employed, where the system kinematics is described only through the displacement of points on the movable electrode mid-surface, see for example Timoshenko (1970). The actual distance g between the two electrodes is therefore given by $g_0 + w$, where g_0 is the initial gap. Linear and nonlinear microplates have been studied by Francais and Dufour (1999), Ng et al. (2004), Zhao et al. (2004), Vogl and Nayfeh (2005), Batra et al. (2008a), Porfiri (2008). When the bending stiffness of the deformable electrode is negligible compared to its in-plane stretching and $g_0/\ell \ll 1$, the electrode can be regarded as a linear elastic membrane. The membrane approximation is valid for $\ell/h \geq 400$, see for example Mansfield (1989). Linear micromembranes have been studied by Pelesko (2002), Pelesko et al. (2003), Pelesko and Chen (2003), Batra et al. (2006a). As discussed by Pelesko (2002), the plate and the membrane approximations are accurate and reliable for many MEMS devices such as micro-pumps made of thin glassy polymers and grating light valves comprised of stretched thin ribbons.

With the decrease in electrostatic MEMS dimensions from the micro to the nanoscale additional nanoscale surface forces, such as the Casimir force and the van der Waals force (Lamoreaux, 2005, Bordag et al., 2001, Lifshitz, 1956, Klimchitskaya et al., 2000), should be considered, see for example Zhao et al. (2003), Lin and Zhao (2007). At small scales, the nanoscale surface forces may overcome elastic restoring actions in the device and lead to the plates' sticking during the fabrication process. van der Waals force and Casimir force can both be connected with the existence of zero-point vacuum oscillations of the electromagnetic field (Bordag et al., 2001, Lifshitz, 1956, Klimchitskaya et al., 2000). The microscopic approach to the modeling of both van der Waals and Casimir forces can be formulated in a unified way using Quantum Field Theory, see for example Lamoreaux (2005), Bordag et al. (2001), Lifshitz (1956), Klimchitskaya et al. (2000). It is found that the Casimir force is generally effective at larger separation distances between the bodies than the van der Waals force. Whereas the Casimir force between semi-infinite parallel plates is inversely proportional to the fourth power of the gap, van der Waals force is inversely proportional to the third power of the gap. The dependence of these forces on the dielectric properties of the plates and the filling medium is studied in detail by Bordag et al. (2001, Section 4.1.1). It is important to note that van der Waals and Casimir forces cannot in general be considered to simultaneously act in MEMS, since they describe the same physical phenomenon at two different length scales. Effect of van der Waals force on the pull-in instability of electrostatically actuated rectangular microplates has been studied by Batra et al. (2008c).

In order to alleviate difficulties associated with the analysis of distributed nonlinear systems, considerable efforts have been devoted to the development of reliable reduced-order models for MEMS. A simple lumped spring-mass system for estimating pull-in parameters is proposed by Nathanson et al. (1967), where the elasticity of the deformable body is lumped into the stiffness of a linear spring. The pull-in voltage so obtained usually exceeds that observed experimentally for many applications (Pamidighantam et al., 2002), and the pull-in displacement always equals one-third of the initial gap. Moreover, the aforesaid description does not incorporate inherent nonlinearities of the electrostatic, the Casimir, and the restoring forces (Chu et al., 1996, Castañer and

Senturia, 1999). A reduced-order model for microplates that accounts for the mid-plane stretching and the non-linearity in the electrostatic force has been used by Zhao et al. (2004) to study pull-in instability and natural frequencies of a plate predeformed by an electric field. Pamidighantam et al. (2002) have studied microbeams through a reduced one degree-of-freedom (d.o.f.) model which improves the pull-in voltage estimate of the lumped system of Nathanson et al. (1967); however, the pull-in displacement is empirically chosen. Multimode analysis on microbeams using a nonlinear beam equation has been done by Abdel-Rahman et al. (2002), Zhang and Zhao (2006), where the effect of the number of modes retained in the trial solution on its convergence is investigated. Batra et al. (2006c) used a one d.o.f. model to extract pull-in parameters of a narrow microbeam. This reduced-order model accounts for the mid-plane stretching and fringing fields in the electrostatic load, and it is obtained by using the static deflection of the beam under a uniformly distributed load as the trial solution in the Galerkin method. Batra et al. (2008b) showed that this reduced-order model predicts well the pull-in parameters when the mode shape corresponding to the fundamental frequency is taken as the basis function. Furthermore, predictions from this model agree well with results from the solution of the three-dimensional problem by the finite element method. Reduced-order models have also been used to study the sticking phenomenon in nano-electromechanical systems (NEMS) due to the Casimir force. Serry et al. (1998), Ding et al. (2001) studied a rectangular membrane using the 1D distributed model and considering nonlinear stretching effects; while Bárcenas et al. (2005) used a lumped one d.o.f. model to analyze the stiction phenomenon between two conductors made of different materials. Lin and Zhao (2005) studied the effect of Casimir force on pull-in parameters of NEM switches by obtaining an approximate analytical expression of the critical pull-in gap by the perturbation theory. The literature on electrostatically actuated MEMS has been reviewed by Batra et al. (2007b).

Here, we propose a reduced-order model for studying the pull-in instability and the fundamental frequency of clamped microplates under the combined effects of the Coulomb and the Casimir forces. The large transverse displacement, moderate rotations, and small strains plate theory, see Landau and Lifshitz (1986), is used by incorporating the von Kármán nonlinearity in the mechanical model following the work reported by Younis et al. (2003). Since small strains are involved, we use the parallel plate approximation for the Coulomb force, and the proximity force approximation for the Casimir force. We note that both these approximations are consistent with the approximation of locally parallel conductors. Thus, the dependence of the Casimir force on the spatial derivatives of the gap g is neglected. Assuming that in-plane dimensions of supports holding the MEMS edges fixed are very large as compared to those of the MEMS, we neglect the effects of fringing fields in the electrostatic force.

We consider rectangular and circular MEMS, and use the Galerkin method with different kinematically admissible trial solutions to reduce the governing 2D nonlinear boundary-value problem to a nonlinear algebraic problem where both the pull-in voltage and the pull-in displacement are treated as unknowns. For the static problem, pull-in parameters are found by using the displacement iteration pull-in extraction algorithm proposed by Bochobza-Degani et al. (2002). Eigenvalue problems corresponding to linear vibrations of the system about its deflected position are solved for the fundamental frequency. It is shown that the fundamental frequency goes to zero as pull-in conditions are approached. The pull-in parameters found from the eigenvalue analysis agree well with those derived from the static analysis. Convergence studies with an increase in the number of basis functions reveal that 9 (4) basis functions for a rectangular (circular) plate give a converged solution, and 3 (2) basis functions give values of pull-in parameters with less than 5% error. In the absence of the applied electrostatic force, the value of the nanoscale surface force corresponding to the pull-in instability determines the device size that can be safely fabricated. Reduced-order models for linear rectangular and circular membranes are obtained as special cases.

The rest of the paper is organized as follows. In Sections 2 and 3, we describe, respectively, the electromechanical and the reduced-order models for a von Kármán plate under the effect of the Coulomb and the nanoscale surface forces. The derivation of the reduced-order model follows a procedure typically used for studying deformations of thin-walled structures. That is, in-plane inertial effects are neglected, and the resulting equation is solved for in-plane displacements in terms of transverse deflections which are then substituted in the equation governing the evolution of transverse deflection. Once transverse deflections have been computed, in-plane displacements can be found. In Section 4, we briefly outline the technique used to solve equations for the reduced-order model. In Section 5, we present results, that is pull-in parameters and fundamental frequencies for microplates and micromembranes, and we investigate the effect of the Casimir force on the pull-in instability and the lowest frequency. Conclusions are summarized in Section 6.

2. Formulation of the initial-boundary-value problem

Referring to the geometry in Fig. 1, we assume that the deformable electrode in the undeformed configuration is a plate-like body occupying the region $\Omega \times (-h/2, h/2)$, and that the initial gap g_0 between the two conductors and the thickness h of the deformable plate are much smaller than its characteristic length ℓ . Thus, Ω is the mid-surface of the plate. In our formulation, g_0 and h can potentially be of the same order of magnitude. We use the von Kármán plate theory to account for large deflections, moderate rotations, and small strains, see for example Landau and Lifshitz (1986). Neglecting the effect of the rotatory inertia, the von Kármán plate equations are, see Landau and Lifshitz (1986)

$$\rho h \ddot{w} + D \Delta \Delta w - h \operatorname{div}(\boldsymbol{\sigma} \nabla w) - F_e - F_C = 0, \tag{1a}$$

$$\rho \ddot{\mathbf{u}} - \operatorname{div} \boldsymbol{\sigma} = \mathbf{0}, \tag{1b}$$

where $D = Eh^3/(12(1 - \nu^2))$ is the bending stiffness of the plate; ρ , E , and ν are the mass density, Young’s modulus, and Poisson’s ratio of the plate material, that is assumed to be homogeneous and isotropic; \mathbf{u} and w are the in-plane and the out-of-plane displacements of a point on the mid-surface; $\boldsymbol{\sigma}$ is the in-plane stress tensor; F_e and F_C are the Coulomb and the Casimir forces; Δ , div , and ∇ are the Laplace, the divergence, and the gradient operators with respect to the curvilinear in-plane coordinates x^1 and x^2 , see Fig. 1; and a superimposed dot means partial time derivative. Expressions for the Coulomb and the Casimir forces are discussed below. Eqs. (1) and others given below are written in direct notation. Definitions of differential operators in curvilinear coordinates are given in Appendix B.

We note that when $\boldsymbol{\sigma} = \sigma_0 \mathbf{1}$, where σ_0 is a constant having dimensions of the stress and $\mathbf{1}$ is the 2D identity tensor, and the rigidity due to in-plane stretching dominates over the bending stiffness in supporting the external load, Eqs. (1) reduce to equations governing deformations of a linear elastic membrane.

In the von Kármán plate theory, the in-plane strain tensor $\boldsymbol{\varepsilon}$ is given by

$$\boldsymbol{\varepsilon} = \operatorname{sym} \nabla \mathbf{u} + \frac{1}{2} \nabla w \otimes \nabla w, \tag{2}$$

where $\operatorname{sym} \nabla \mathbf{u}$ is the symmetric part of $\nabla \mathbf{u}$ and \otimes denotes the tensor product between two vector fields (see Appendix A). Assuming the response of the material to be linear elastic with the prestress $\sigma_0 \mathbf{1}$ in the reference configuration, the constitutive relation under the Kirchhoff assumption (see Batra, 2005) is:

$$\boldsymbol{\sigma} = \frac{E}{1 + \nu} \left(\boldsymbol{\varepsilon} + \frac{\nu}{1 - \nu} (\operatorname{tr} \boldsymbol{\varepsilon}) \mathbf{1} \right) + \sigma_0 \mathbf{1}, \tag{3}$$

where $\operatorname{tr} \boldsymbol{\varepsilon}$ is the trace of $\boldsymbol{\varepsilon}$. Substitution for $\boldsymbol{\sigma}$ from Eq. (3) into Eqs. (1), assuming that σ_0 is constant, and using Eq. (2) and identity (A.5) in Appendix A, give the following equations for \mathbf{u} and w :

$$\rho h \ddot{w} + D \Delta \Delta w - B \operatorname{div} \left[((1 - \nu) \operatorname{sym} \nabla \mathbf{u} + \nu (\operatorname{div} \mathbf{u}) \mathbf{1}) \nabla w + \frac{1}{2} (\nabla w \cdot \nabla w) \nabla w \right] - \sigma_0 h \Delta w - F_e - F_C = 0, \tag{4a}$$

$$\rho h \ddot{\mathbf{u}} - \frac{B}{2} ((1 - \nu) \Delta \mathbf{u} + (1 + \nu) \nabla \operatorname{div} \mathbf{u}) = \frac{B}{2} ((1 - \nu) \operatorname{div} (\nabla w \otimes \nabla w) + \nu \nabla (\nabla w \cdot \nabla w)), \tag{4b}$$

where $B = Eh/(1 - \nu^2)$, and $\mathbf{a} \cdot \mathbf{b}$ indicates the inner product between vectors \mathbf{a} and \mathbf{b} .

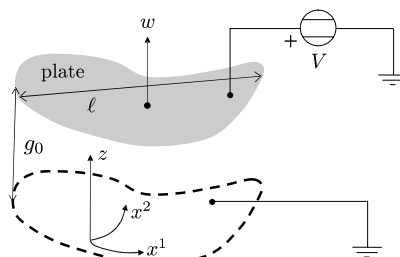


Fig. 1. Sketch of the electrostatically actuated device.

From an electrical point of view, the system depicted in Fig. 1 behaves as a variable gap capacitor. By assuming that $g_0/\ell \ll 1$ and by neglecting fringing fields due to reasons explained in Section 1, the magnitude F_e of the electrostatic force acting on the deformable electrode along its normal is given by, see Pelesko and Bernstein (2002),

$$F_e = -\frac{\epsilon_0 V^2}{2g_0^2(1 + \hat{w})^2}, \quad (5)$$

where $\hat{w} = w/g_0$ is the nondimensional transverse displacement, ϵ_0 is the dielectric constant in vacuum, and V is the applied direct current voltage. Therefore, the expression for the electrostatic force depends only on the gap g . Thus, the validity of the analysis is limited to those variable gap capacitors whose actual gap is differentially uniform, that is, the two conductors are locally parallel to each other, see for example Pelesko and Bernstein (2002). Also, because of small strains and moderate rotations involved, the force F_e is assumed to act along the normal to the undeformed plate.

We use the proximity force approximation (PFA) for the Casimir force F_C that is consistent with assumptions made in the mechanical and the electrostatic models. In the PFA, curved surfaces are viewed as a superimposition of infinitesimal parallel plates; see for example Bordag (2006), Gies and Klingmüller (2006) and references therein. Gies and Klingmüller (2006) have shown that for a sphere of radius ℓ separated from a flat plate by a distance g , the PFA gives results within 1% accuracy for $g/\ell < 0.1$. For perfect conductors, the PFA approximation gives

$$F_C = -\frac{\hbar c \pi^2}{240g_0^4(1 + \hat{w})^4}, \quad (6)$$

where \hbar is Planck's constant and c the speed of light in vacuum. For nonperfect conductors, the Casimir force is still inversely proportional to g_0^4 , but the proportionality constant differs from that in Eq. (6), see for example Bordag et al. (2001). Corrections to Eq. (6) for geometries with known and fixed departures from the parallel configurations are given in Bordag (2006), Gies and Klingmüller (2006). However, Eq. (6) is consistent with the parallel plate approximation for the electrostatic force, and the small deformations assumption in the mechanical model. For gaps smaller than the retardation length, that is, for gaps smaller than the wavelength of the virtual transitions responsible for the quantum dipole fluctuations (Bordag et al., 2001, Klimchitskaya et al., 2000), the nanoscale interaction between the two bodies is described by the van der Waals distributed force per unit surface area, see for example Israelachvili (1991), Laliotis et al. (2007), Zhao et al. (2003):

$$F_{\text{vdW}} = -\frac{H}{6\pi g_0^3(1 + \hat{w})^3}. \quad (7)$$

In Eq. (7), H is the Hamaker constant with values in the range $[0.4, 4] \times 10^{-19}$ J.

van der Waals and Casimir forces between parallel layered metallic surfaces have been extensively studied in the literature, see for example, Bordag et al. (2001), Klimchitskaya et al. (2000). For gold-coated aluminum surfaces, it is found that van der Waals force, see Eq. (7), is effective in the gap range 0.5–4 nm. For gaps in the range 4 nm–1 μm , there is a transition between the force-distance dependence g^{-3} (van der Waals force) to the force-distance dependence g^{-4} (Casimir force). For gaps larger than 1 μm , the interaction between the plates is described by the Casimir force, see Eq. (6). Therefore, for perfect conductors, at large separation distances the interaction force is independent of the material properties of plates, whereas, as the gap decreases, the interaction force is affected by the material properties of the system. For dielectric bodies, the van der Waals force is effective at larger distances as shown by Israelachvili and Tabor (1972).

In this work, we consider the Casimir force given by Eq. (6). Therefore, the analysis applies to those MEMS devices with separation distances $\gtrsim 1 \mu\text{m}$. The analysis with an expression for the nanoscale surface force valid in the transition range between Casimir and van der Waals force is left for future work. The effect of van der Waals force and thermal stresses on pull-in parameters of a rectangular plate has been studied by Batra et al. (2008c).

For convenience we introduce the nondimensional time $\hat{t} = t/\tau$, where

$$\tau^2 = \frac{12\alpha\ell^4}{Eh^2}(1 - \nu^2), \tag{8}$$

and the in-plane displacement $\hat{\mathbf{u}} = \mathbf{u}\ell/g_0^2$. We use a superimposed dot to denote time derivative with respect to \hat{t} . Also, we drop the superimposed hat on nondimensional variables. Thus, Eqs. (4) become

$$\ddot{w} + \Delta\Delta w - 12\alpha\text{div} \left[((1 - \nu)\text{sym}\nabla\mathbf{u} + \nu(\text{div}\mathbf{u})\mathbf{1})\nabla w + \frac{1}{2}(\nabla w \cdot \nabla w)\nabla w \right] - \beta\Delta w + \frac{\lambda}{(1+w)^2} + \frac{\mu}{(1+w)^4} = 0, \tag{9a}$$

$$\gamma\ddot{\mathbf{u}} - (1 - \nu)\Delta\mathbf{u} - (1 + \nu)\nabla\text{div}\mathbf{u} = (1 - \nu)\text{div}(\nabla w \otimes \nabla w) + \nu\nabla(\nabla w \cdot \nabla w), \tag{9b}$$

where

$$\alpha = \frac{g_0^2}{h^2}, \quad \beta = 12\frac{\sigma_0\ell^2}{Eh^2}(1 - \nu^2), \quad \gamma = \frac{h^2}{6\ell^2}, \quad \lambda = \frac{6\epsilon_0 V^2 \ell^4}{Eh^3 g_0^3}(1 - \nu^2), \quad \mu = \frac{\hbar c \pi^2 \ell^4}{20Eh^3 g_0^5}(1 - \nu^2). \tag{10}$$

Nondimensional parameters β , λ , and μ are indicators of the MEMS stiffening due to the initial stress, the Coulomb force, and the Casimir force, respectively. We assume that the order of magnitude of different terms in Eqs. (9) is determined by the order of the corresponding nondimensional parameters. Since von Kármán approximation holds for $h/\ell \ll 1$, therefore $\gamma \ll 1$, we neglect the inertial term in Eq. (9b) and obtain its following simplified form

$$(1 - \nu)\Delta\mathbf{u} + (1 + \nu)\nabla\text{div}\mathbf{u} = -(1 - \nu)\text{div}(\nabla w \otimes \nabla w) - \nu\nabla(\nabla w \cdot \nabla w). \tag{11}$$

We consider the boundary Γ of Ω to be clamped. The kinematic boundary conditions for a clamped edge are, see Meirovitch (1967)

$$w = 0 \quad \text{and} \quad \nabla w \cdot \mathbf{n} = 0, \tag{12a}$$

$$\mathbf{u} = \mathbf{0}, \tag{12b}$$

where \mathbf{n} is the outward unit normal vector field on Γ that lies in the mid-surface of the plate.

We do not study transient behavior of microplates, but only static deformations or steady state vibrations. Therefore, we do not need to prescribe initial conditions.

3. Reduced-order system

A closed-form solution of the initial-boundary-value problem defined by Eqs. (9a) and (11) and boundary conditions (12a) and (12b) cannot be found. An approximate solution is constructed by expressing the displacement fields \mathbf{u} and w as

$$w(x^1, x^2, t) = \sum_{n=1}^N \bar{w}_n(x^1, x^2)\zeta_n(t) = \mathbf{W}^T(x^1, x^2)\boldsymbol{\zeta}(t), \tag{13a}$$

$$\mathbf{u}(x^1, x^2, t) = \sum_{p=1}^P \bar{\mathbf{u}}_p(x^1, x^2)\xi_p(t) = \mathbf{U}^T(x^1, x^2)\boldsymbol{\xi}(t), \tag{13b}$$

where \bar{w}_n and $\bar{\mathbf{u}}_p$ are orthogonal basis functions for the transverse and the in-plane displacements, and ζ_n and ξ_p are the corresponding amplitude parameters or equivalently the mode participation factors. Basis functions are collected into the N -vector \mathbf{W} and into the P -vector \mathbf{U} , and amplitudes are collected into the N -vector $\boldsymbol{\zeta}$ and into the P -vector $\boldsymbol{\xi}$. Each basis function satisfies the corresponding kinematic boundary conditions, that is, Eqs. (12a) and (12b).

3.1. Basis functions for in-plane displacement

A basis function for the in-plane displacement is determined by solving the following linear eigenvalue problem associated with Eq. (9b):

$$\kappa^2 \bar{\mathbf{u}}_p + (1 - \nu) \Delta \bar{\mathbf{u}}_p + (1 + \nu) \nabla \operatorname{div} \bar{\mathbf{u}}_p = \mathbf{0}, \quad (14)$$

where κ is the wave number. We decompose the in-plane displacement as $\mathbf{u} = \mathbf{u}^n + \mathbf{u}^t$, where \mathbf{u}^n and \mathbf{u}^t are displacement vectors for longitudinal and transverse waves satisfying $\operatorname{curl} \mathbf{u}^n = \mathbf{0}$ and $\operatorname{div} \mathbf{u}^t = 0$, respectively. Therefore, Eq. (14) is equivalent to the following two equations, see for example Landau and Lifshitz (1986):

$$\Delta \bar{\mathbf{u}}^n + \eta_n^2 \bar{\mathbf{u}}^n = \mathbf{0}, \quad (15a)$$

$$\Delta \bar{\mathbf{u}}^t + \eta_t^2 \bar{\mathbf{u}}^t = \mathbf{0}, \quad (15b)$$

where $\eta_n = \kappa/\sqrt{2}$ and $\eta_t = \kappa/\sqrt{1 - \nu}$ are the wave numbers of the longitudinal and the transverse waves, respectively.

Since $\operatorname{curl} \bar{\mathbf{u}}^n = \mathbf{0}$, we solve Eq. (15a) by introducing the scalar potential ϕ through $\bar{\mathbf{u}}^n = \nabla \phi$. Therefore, within an arbitrary additive constant Eq. (15a) reduces to

$$\Delta \phi + \eta_n^2 \phi = 0. \quad (16)$$

In order to solve Eq. (15b), we introduce the vector potential Φ through $\bar{\mathbf{u}}^t = \operatorname{curl} \Phi$. The fact that $\bar{\mathbf{u}}^t$ is an in-plane vector field in Ω and Eq. (B.13) imply that $\Phi = \Phi \mathbf{g}_3$, where \mathbf{g}_3 is the normal vector field in the z coordinate direction (see Fig. 1) and Φ is a scalar field in Ω . Therefore, within an arbitrary additive vector field $\tilde{\Phi}$ such that $\operatorname{curl} \tilde{\Phi} = \mathbf{0}$, the eigenvalue problem (15b) reduces to

$$\Delta \Phi + \eta_t^2 \Phi = 0. \quad (17)$$

By integrating over the domain Ω and by applying Green's formulas to transform surface integrals into line integrals, conditions $\operatorname{curl} \bar{\mathbf{u}}^n = \mathbf{0}$ and $\operatorname{div} \bar{\mathbf{u}}^t = 0$ imply the following set of boundary conditions for the displacements associated with the longitudinal and the transverse waves

$$\bar{\mathbf{u}}^n \cdot \mathbf{t} = 0, \quad \bar{\mathbf{u}}^t \cdot \mathbf{n} = 0, \quad (18)$$

where \mathbf{t} is the tangent vector to the boundary Γ of Ω , such that $(\mathbf{n}, \mathbf{t}, \mathbf{g}_3)$ is a positively oriented basis. Additional boundary conditions are provided by Eq. (12b) through

$$\bar{\mathbf{u}}^n \cdot \mathbf{n} = \bar{\mathbf{u}}^t \cdot \mathbf{n} = 0, \quad \bar{\mathbf{u}}^t \cdot \mathbf{t} = \bar{\mathbf{u}}^n \cdot \mathbf{t} = 0. \quad (19)$$

We note that the governing equations for the potentials ϕ and Φ , that is, Eqs. (16) and (17), respectively, are equivalent. Nevertheless, the normal and transverse displacement fields are generally different since the relation between them and their corresponding potential are different.

3.2. Relation between ξ and ζ

In order to express ξ in terms of ζ , we substitute from Eqs. (13) into Eq. (11), take the inner product of both sides of the resulting equation with the in-plane mode $\bar{\mathbf{u}}_p$, and integrate over the domain Ω . Applying identities given in Appendix A, the divergence theorem and imposing boundary condition (12b) on the boundary integrals we obtain

$$\xi_p = \zeta^T \mathbf{H}_p \zeta, \quad (20)$$

where the $(N \times N)$ symmetric matrix \mathbf{H}_p is given by

$$[\mathbf{H}_p]_{mn} = - \int_{\Omega} ((1 - \nu) \nabla^T \bar{\mathbf{u}}_p \nabla \bar{w}_m \cdot \nabla \bar{w}_n + \nu (\nabla \bar{w}_m \cdot \nabla \bar{w}_n) \operatorname{div} \bar{\mathbf{u}}_p) \, d\Omega \left(\int_{\Omega} ((1 - \nu) \operatorname{tr}(\nabla \bar{\mathbf{u}}_p \nabla^T \bar{\mathbf{u}}_p) + (1 + \nu) (\operatorname{div} \bar{\mathbf{u}}_p)^2) \, d\Omega \right)^{-1}, \quad m, n = 1, \dots, N. \quad (21)$$

Formulae to compute the gradient of a vector field in curvilinear coordinates are given in Appendix B.

We note that all amplitude coefficients for the transverse displacement are needed for computing any amplitude coefficient of the in-plane displacement field. In addition, we note that relation (11) between the in-plane motion and the transverse motion is nonlinear and that the in-plane motion vanishes in the linear theory. Because of the P internal constraints (20), the reduced-order model for the microplate has N degrees of freedom.

3.3. Equations for the reduced-order system

The reduced-order model is obtained by premultiplying both sides of Eq. (9a) with \mathbf{W} , substituting for w and \mathbf{u} from Eqs. (13), integrating the resulting equation over Ω , and substituting into it the relation (20):

$$\int_{\Omega} \mathbf{W}\mathbf{W}^T \ddot{\zeta} \, d\Omega + \int_{\Omega} \mathbf{W}\Delta\Delta\mathbf{W}^T \zeta \, d\Omega - 12\alpha \int_{\Omega} \mathbf{W} \operatorname{div} \left(\bar{\mathbf{e}} \nabla \mathbf{W}^T \zeta + \frac{1}{2} (\nabla \mathbf{W}^T \zeta \cdot \nabla \mathbf{W}^T \zeta) \nabla \mathbf{W}^T \zeta \right) \, d\Omega - \beta \int_{\Omega} \mathbf{W}\Delta\mathbf{W}^T \zeta + \lambda \int_{\Omega} \frac{\mathbf{W}}{(1 + \mathbf{W}^T \zeta)^2} \, d\Omega + \mu \int_{\Omega} \frac{\mathbf{W}}{(1 + \mathbf{W}^T \zeta)^4} \, d\Omega = \mathbf{0}, \tag{22}$$

where

$$\bar{\mathbf{e}} = \sum_{p=1}^P \xi_p(\zeta) \mathbf{E}_p = \sum_{p=1}^P (\zeta^T \mathbf{H}_p \zeta) \mathbf{E}_p, \tag{23a}$$

$$\mathbf{E}_p = (1 - \nu) \operatorname{sym} \nabla \bar{\mathbf{u}}_p + \nu (\operatorname{div} \bar{\mathbf{u}}_p) \mathbf{1}. \tag{23b}$$

We now define the following $(N \times N)$ matrices

$$[\mathbf{D}]_{mn} = \nabla \bar{w}_m \cdot \nabla \bar{w}_n, \quad [\mathbf{L}]_{mn} = \Delta \bar{w}_m \Delta \bar{w}_n, \quad [\mathbf{G}]_{mn} = \bar{\mathbf{e}} \nabla \bar{w}_m \cdot \nabla \bar{w}_n, \quad m, n = 1, \dots, N. \tag{24}$$

Using the divergence theorem and imposing boundary conditions (12a) we obtain the following equation for the reduced-order system:

$$\mathbf{m} \ddot{\zeta} + (\mathbf{k}_1 + \beta \mathbf{k}_2 + \alpha \mathbf{k}_3(\zeta)) \zeta + \lambda \mathbf{f}_e(\zeta) + \mu \mathbf{f}_c(\zeta) = \mathbf{0}, \tag{25}$$

where

$$\mathbf{m} = \int_{\Omega} \mathbf{W}\mathbf{W}^T \, d\Omega, \tag{26a}$$

$$\mathbf{k}_1 = \int_{\Omega} \mathbf{L} \, d\Omega, \quad \mathbf{k}_2 = \int_{\Omega} \mathbf{D} \, d\Omega, \tag{26b}$$

$$\mathbf{k}_3(\zeta) = 12 \int_{\Omega} \left(\mathbf{G} + \frac{1}{2} (\zeta^T \mathbf{D} \zeta) \mathbf{D} \right) \, d\Omega, \tag{26c}$$

$$\mathbf{f}_e(\zeta) = \int_{\Omega} \frac{\mathbf{W}}{(1 + \mathbf{W}^T \zeta)^2} \, d\Omega, \quad \mathbf{f}_c(\zeta) = \int_{\Omega} \frac{\mathbf{W}}{(1 + \mathbf{W}^T \zeta)^4} \, d\Omega. \tag{26d}$$

In Eq. (25), $\mathbf{k}_1 + \beta \mathbf{k}_2$ represents the stiffness of a linear elastic plate, and $\alpha \mathbf{k}_3(\zeta)$ the strain-stiffening effect.

We note that the system represented by Eq. (25) depends on N displacement unknowns. As will be shown below, $N = 1$ gives very good results. However, Eqs. (26) involve \mathbf{G} that depends upon $\bar{\mathbf{e}}$ given by Eq. (23a). Thus the total number of basis functions equals $N + P$.

4. Extraction of pull-in parameters, and frequencies of a deformed plate

4.1. Solution of the static problem

For the static problem, we assume that the voltage difference is applied slowly to the two electrodes, and neglect the inertia term in Eq. (25).

The tangent stiffness matrix of the reduced-order system is given by

$$\mathbf{K}(\zeta, \alpha, \beta, \lambda, \mu) = \mathbf{k}_1 + \beta \mathbf{k}_2 + \alpha \left(\mathbf{k}_3(\zeta) + \frac{d\mathbf{k}_3(\zeta)}{d\zeta} \zeta \right) + \lambda \frac{d\mathbf{f}_c(\zeta)}{d\zeta} + \mu \frac{d\mathbf{f}_C(\zeta)}{d\zeta}, \tag{27}$$

where

$$\frac{d\mathbf{f}_c(\zeta)}{d\zeta} = -2 \int_{\Omega} \frac{\mathbf{W}\mathbf{W}^T}{(1 + \mathbf{W}^T\zeta)^3} d\Omega, \quad \frac{d\mathbf{f}_C(\zeta)}{d\zeta} = -4 \int_{\Omega} \frac{\mathbf{W}\mathbf{W}^T}{(1 + \mathbf{W}^T\zeta)^5} d\Omega. \tag{28}$$

Using the linearity of the trace operator, from Eqs. (23a) and (24) we obtain

$$\frac{d[\mathbf{G}]_{mn}}{d\zeta} \zeta = \left[\sum_{p=1}^P 2\text{tr}(\mathbf{E}_p \nabla \bar{w}_m \otimes \nabla \bar{w}_n) \zeta^T \mathbf{H}_p \right] \zeta = 2 \sum_{p=1}^P (\mathbf{E}_p \nabla \bar{w}_m \cdot \nabla \bar{w}_n) (\zeta^T \mathbf{H}_p \zeta) = 2[\mathbf{G}]_{mn}, \tag{29}$$

and similarly

$$\frac{d(\zeta^T \mathbf{D} \zeta) [\mathbf{D}]_{mn}}{d\zeta} \zeta = 2(\zeta^T \mathbf{D} \zeta) [\mathbf{D}]_{mn}. \tag{30}$$

Therefore, Eq. (27) becomes

$$\mathbf{K}(\zeta, \alpha, \beta, \lambda, \mu) = \mathbf{k}_1 + \beta \mathbf{k}_2 + 3\alpha \mathbf{k}_3(\zeta) + \lambda \frac{d\mathbf{f}_c(\zeta)}{d\zeta} + \mu \frac{d\mathbf{f}_C(\zeta)}{d\zeta}. \tag{31}$$

At the onset of instability the system’s tangent stiffness matrix becomes singular. Therefore, at pull-in the system satisfies Eq. (25) with $\ddot{\zeta} = \mathbf{0}$, and the condition $\det \mathbf{K}(\zeta, \alpha, \beta, \lambda, \mu) = 0$.

When the static problem is solved for $\lambda = 0$ it gives the critical value, μ_{cr} , of the Casimir force parameter at which the pull-in instability occurs. When $\mu = \mu_{cr}$ the system collapses spontaneously with zero applied voltage. Thus such a MEMS cannot be fabricated. The effect of the MEMS size on pull-in parameters λ_{PI} and $\|w_{PI}\|_{\infty}$ is investigated by solving Eq. (25) with $\ddot{\zeta} = \mathbf{0}$ and variable λ for different values of μ in the range $[0, \mu_{cr}]$. The pull-in instability $(\lambda_{PI}, \|w_{PI}\|_{\infty})$ occurs when the curve $\|w\|_{\infty}(\lambda, \mu)$ becomes multivalued. Here $\|w_{PI}\|_{\infty}$ equals the maximum transverse displacement of a plate particle at the onset of the pull-in instability.

We use the displacement iteration pull-in extraction (DIPIE) algorithm (Bochobza-Degani et al., 2002) to solve Eq. (25) with $\ddot{\zeta} = \mathbf{0}$. It enables one to find the complete bifurcation path by driving the system through the displacement of a pre-chosen point $(\bar{x}^1, \bar{x}^2) \in \Omega$, treating the load parameter (either λ or μ) as unknown. The method is explained for the case of variable λ and fixed μ . When studying the behavior of the system under the effect of either the Casimir or the van der Waals force only, that is, for $\lambda = 0$ with varying μ , exactly the same procedure applies except that the role of the two parameters is exchanged.

A parameter s , representing the deflection of a point $(\bar{x}^1, \bar{x}^2) \in \Omega$, is added. Both ζ and λ are regarded as functions of s . If the solution $(\zeta_{i-1}, \lambda_{i-1})$ corresponding to $\mathbf{W}^T(\bar{x}^1, \bar{x}^2) \zeta_{i-1} = s_{i-1}$ is known, the solution $(\zeta_i, \lambda_i) = (\zeta_{i-1}, \lambda_{i-1}) + (\Delta \zeta_i, \Delta \lambda_i)$ corresponding to $s_i = s_{i-1} + \Delta s_i$ is obtained by solving the following system of equations:

$$(\mathbf{k}_1 + \beta \mathbf{k}_2 + \alpha \mathbf{k}_3(\zeta_i)) \zeta_i + \lambda_i \mathbf{f}_c(\zeta_i) + \mu \mathbf{f}_C(\zeta_i) = \mathbf{0}, \tag{32a}$$

$$\mathbf{W}^T(\bar{x}^1, \bar{x}^2) \zeta_i = s_i. \tag{32b}$$

The solution of the set of nonlinear Eqs. (32) in terms of the unknowns $\Delta \zeta_i$ and $\Delta \lambda_i$ is found by using Newton’s iterations. Hence, at the generic j th iteration

$$\begin{bmatrix} \mathbf{K}(\zeta_i^{(j)}, \lambda_i^{(j)}, \mu) & \frac{d\mathbf{f}_c(\zeta_i^{(j)})}{d\zeta} \\ \mathbf{W}^T(\bar{x}^1, \bar{x}^2) & \mathbf{0} \end{bmatrix} \begin{bmatrix} \Delta \zeta_i^{(j)} \\ \Delta \lambda_i^{(j)} \end{bmatrix} = - \begin{bmatrix} (\mathbf{k}_1 + \mathbf{k}_2 + \mathbf{k}_3(\zeta_i^{(j)})) \zeta_i^{(j)} + \lambda_i^{(j)} \mathbf{f}_c(\zeta_i^{(j)}) + \mu \mathbf{f}_C(\zeta_i^{(j)}) \\ \mathbf{W}^T(\bar{x}^1, \bar{x}^2) \zeta_i^{(j)} - s_i \end{bmatrix}, \tag{33}$$

where $(\Delta \zeta_i^{(j)}, \Delta \lambda_i^{(j)})$ indicates the j th solution increment; $(\zeta_i^{(j)}, \lambda_i^{(j)})$ is the updated solution at the $(j - 1)$ th iteration, that is,

$$\zeta_i^{(j)} = \zeta_{i-1} + \sum_{k=1}^{j-1} \Delta\zeta_i^{(k)}, \quad \lambda_i^{(j)} = \lambda_{i-1} + \sum_{k=1}^{j-1} \Delta\lambda_i^{(k)}. \tag{34}$$

The iterations are performed until

$$\max[|\Delta\zeta_i^{(j)}|, \Delta\lambda_i^{(j)}] \leq \epsilon_T, \tag{35}$$

where ϵ_T is a preassigned small number.

4.2. Frequencies of an electrostatically loaded MEMS

For given values of α , β , and μ , and for every converged solution (ζ_i, λ_i) of the static problem up to pull-in, we perturb the static solution by setting $\zeta_{i+1} = \zeta_i + \Delta\zeta_i \exp(i\omega t)$ in Eq. (25) and linearize it around (ζ_i, λ_i) . Here $\Delta\zeta_i$ is a constant vector, $i = \sqrt{-1}$, and ω is the natural frequency of free vibration of the deformed plate that is obtained by solving the following eigenvalue problem:

$$\det(\mathbf{K}(\zeta_i, \alpha, \beta, \lambda_i, \mu) - \omega^2 \mathbf{m}) = 0. \tag{36}$$

Since the tangent stiffness matrix becomes singular at pull-in, it follows that corresponding to pull-in at least one natural frequency of the system equals zero. It is an alternative way of finding the pull-in parameters of the statically deformed plate.

5. Results

Results presented below for clamped rectangular and circular plates have been computed for $\nu = 0.25$. Unless otherwise stated, we apply constant increments $|\Delta s_i| = 10^{-3}$ to extract pull-in parameters with the DIPIE algorithm. Tolerance ϵ_T in Eq. (35) equals 10^{-7} . When $\lambda = 0$, $\mu = 0$ the numerical scheme is started with $s_0 = 0$, consistent with the assumption that the corresponding deflection of every point on the plate’s mid-surface is zero.

We solve the problem for $\lambda = 0$ to determine the critical parameters (ζ_{cr}, μ_{cr}) , corresponding to collapse of the system with zero applied voltage and purely due to the effect of the Casimir force. When solving the problem with variable λ and assigning values to μ in the range $[0, \mu_{cr}]$, the DIPIE scheme is started with $s_0 = \mathbf{W}^T(\bar{x}^1, \bar{x}^2)\zeta_\mu$, where ζ_μ is the converged set of deflection parameters corresponding to $\lambda = 0$ and the assigned value of μ .

5.1. Rectangular plate

We consider a rectangular plate with nondimensional lengths of sides equal to 1 and $\varphi \in]0, 1]$. The two-dimensional region representing the plate’s mid-surface is described in the reference configuration by the rectangular Cartesian coordinate system (x^1, x^2) with x^1 and x^2 axes aligned with sides of lengths 1 and φ , respectively.

Integrals appearing in Eqs. (26) for the reduced-order model for the microplate have been evaluated using the 21×21 Gauss quadrature rule. For the DIPIE algorithm we adopt $(\bar{x}^1, \bar{x}^2) = (1/2, \varphi/2)$ as the point whose displacement s is imposed.

The solution of the eigenvalue problem (14) with the method explained in Section 3.1 gives the following basis functions for the in-plane displacement in Eq. (13b):

$$\bar{\mathbf{u}}_p(x^1, x^2) = A_{r,l} \sin(r\pi x^1) \sin\left(\frac{l\pi x^2}{\varphi}\right) (\mathbf{g}^1 + \mathbf{g}^2) \tag{37}$$

where $A_{r,l}$ are constants used for normalization, and $p = (r - 1)\bar{q} + l$ for $r = 1, \dots, \bar{p}$ and $l = 1, \dots, \bar{q}$.

For the transverse displacement, we use the following set of kinematically admissible basis functions

$$\bar{w}_m(x^1, x^2) = A_m \left(\frac{\cosh(\Lambda_m x^1) - \cos(\Lambda_m x^1)}{\cosh \Lambda_m - \cos \Lambda_m} - \frac{\sinh(\Lambda_m x^1) - \sin(\Lambda_m x^1)}{\sinh \Lambda_m - \sin \Lambda_m} \right) \times \left(\frac{\cosh\left(\frac{\Lambda_m x^2}{\varphi}\right) - \cos\left(\frac{\Lambda_m x^2}{\varphi}\right)}{\cosh \Lambda_m - \cos \Lambda_m} - \frac{\sinh\left(\frac{\Lambda_m x^2}{\varphi}\right) - \sin\left(\frac{\Lambda_m x^2}{\varphi}\right)}{\sinh \Lambda_m - \sin \Lambda_m} \right), \tag{38}$$

where $\Lambda_m, m = 1, \dots, N$, is the m th root of the transcendental equation

$$\cosh \Lambda \cos \Lambda = 1, \tag{39}$$

and the constant A_m is chosen by normalizing \bar{w}_m with respect to its maximum value. Basis functions (38) equal products of basis functions for clamped–clamped Euler beams of length 1 and φ , respectively. However, the same mode shapes in the x^1 - and the x^2 -directions are considered.

Since each function \bar{w}_m in Eq. (38) is symmetric about the axes $x_1 = 1/2$ and $x_2 = \varphi/2$, the basis functions \mathbf{u}_p in Eq. (37) with

$$\text{mod}(\text{mod}(r, 2) + \text{mod}(l, 2), 2) = 0 \tag{40}$$

imply $[\mathbf{H}_p]_{mn} = 0$ in Eq. (21). Here, $\text{mod}(r, l)$ gives the remainder in the division of r by l . Therefore, the number of basis functions in Eq. (13b) is given by

$$P = \frac{1}{2}(\bar{p}\bar{q} - \text{mod}(\bar{p}\bar{q}, 2)), \tag{41}$$

where only basis functions \mathbf{u}_p such that $\text{mod}(\text{mod}(l, 2) + \text{mod}(r, 2), 2) = 1$ are considered. Results presented below are computed by selecting $\bar{p} = \bar{q}$.

5.1.1. Pull-in parameters from the static analysis

5.1.1.1. Comparison of results. Table 1 lists pull-in parameters $\|w_{PI}\|_\infty$ and λ_{PI} extracted for $\varphi = 1$ (square plate), $\alpha = 1, \beta = 0, \mu = 0$, and different values of \bar{p} and N in Eqs. (37) and (38). The solution is affected by the number of basis functions for the in-plane displacements, while it is not significantly affected by the number of basis functions used to approximate the transverse displacement. The converged values of pull-in parameters (with $\bar{p} = \bar{q} = 4$ and $N = 1$ or a total of $P + N = 9$ basis functions and 1 degree of freedom) match well with the corresponding ones $\|w_{PI}\|_\infty \approx 0.51$ and $\lambda_{PI} \approx 192$ deduced from Fig. 5 of Zhao et al. (2004) who used the hierarchical finite element method to numerically generate eigenfunctions of a linear clamped plate and used them as basis functions for the displacement field.

The primary reason for needing only one basis function for the transverse deflection and several for the in-plane displacements is that the basis functions for the transverse displacement in Eq. (38) approximate well the deformed shape of the microplate under the distributed Coulomb and Casimir forces. However, more basis functions for the in-plane displacement are needed to reproduce accurately the membrane stress that couples the in-plane and the transverse deformations.

5.1.1.2. Critical value of the Casimir force parameter.

5.1.1.2.1. Zero prestress. In Tables 2 and 3, we list for $\alpha = 1$ the critical Casimir force parameter μ_{cr} and the corresponding infinity norm $\|w_{cr}\|_\infty$ of the pull-in displacement for a square and a rectangular plate with $\varphi = 1/2$. They converge with increasing number of basis functions for the in-plane displacement, and they

Table 1

For $\varphi = 1$, nondimensional pull-in parameters $\|w_{PI}\|_\infty$ and λ_{PI} for different number of basis functions used to approximate the in-plane and the transverse displacements

N	$\ w_{PI}\ _\infty$			λ_{PI}		
	$\bar{p}, \bar{q} = \bar{p}$			$\bar{p}, \bar{q} = \bar{p}$		
	2	4	6	2	4	6
1	0.551	0.535	0.534	203	196	196
3	0.551	0.535	0.534	204	196	196
5	0.551	0.534	0.534	204	196	196

Table 2

For $\varphi = 1$, critical Casimir force parameter μ_{cr} and the corresponding pull-in displacement infinity norm $\|w_{cr}\|_{\infty}$ with different number of basis functions for the in-plane and the transverse displacements

N	$\ w_{cr}\ _{\infty}$ $\bar{p}, \bar{q} = \bar{p}$			μ_{cr} $\bar{p}, \bar{q} = \bar{p}$		
	2	4	6	2	4	6
1	0.315	0.309	0.309	103	101	101
3	0.315	0.309	0.309	103	101	101
5	0.315	0.309	0.309	103	101	101

Table 3

For $\varphi = 1/2$, critical Casimir force parameter μ_{cr} and the corresponding pull-in displacement infinity norm $\|w_{cr}\|_{\infty}$ with different number of basis functions for the in-plane and the transverse displacements

N	$\ w_{cr}\ _{\infty}$ $\bar{p}, \bar{q} = \bar{p}$			μ_{cr} $\bar{p}, \bar{q} = \bar{p}$		
	2	4	6	2	4	6
1	0.316	0.310	0.309	766	755	754
3	0.316	0.310	0.310	766	755	754
5	0.316	0.310	0.310	766	755	754

are essentially unaffected by the number of basis functions used to approximate the transverse displacement. We note that μ_{cr} for the clamped rectangular plate with aspect ratio 1/2 is nearly 7.5 times that for the clamped square plate.

Based on results in Tables 1–3 we henceforth use $\bar{p} = 4$ and $N = 1$ in Eqs. (37) and (38). Thus the reduced-order model has $P = 8$ basis functions for the in-plane displacement, $N = 1$ basis functions for the transverse displacement, and $N = 1$ degree of freedom.

For $\lambda = 0$ Fig. 2 shows the variation of the critical Casimir force parameter μ_{cr} with the aspect ratio φ for two values of $\alpha = g_0^2/h^2$. Numerical data in Fig. 2 is interpolated with a fourth order polynomial of the form

$$\mu_{cr} = f(\alpha) \left(1 + \frac{1}{\varphi^2} + \frac{1}{\varphi^4} \right) \tag{42}$$

where the function $f(\alpha)$, plotted in Fig. 3, is given by

$$f(\alpha) = 2.31\alpha + 35.8. \tag{43}$$

Note that μ_{cr} increases rapidly with a decrease in φ . However, for the MEMS to be useful, φ has a lower limit since all four edges are clamped. For two opposite edges clamped and the longer edges kept traction free, the MEMS can be modeled as a beam for which reduced-order models described by Batra et al. (2006c), Batra et al. (2008b) with fringing fields given by Batra et al. (2006b) can be employed.

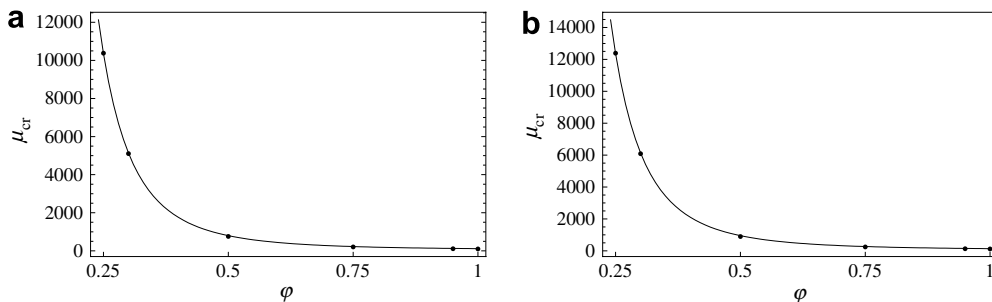


Fig. 2. Variation of μ_{cr} with the aspect ratio φ for (a) $\alpha = 1$ and (b) $\alpha = 4$.

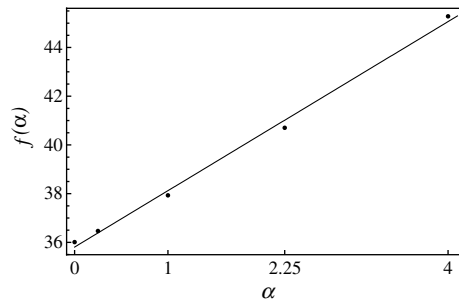


Fig. 3. Variation with α of the function $f(\alpha)$ in Eq. (42).

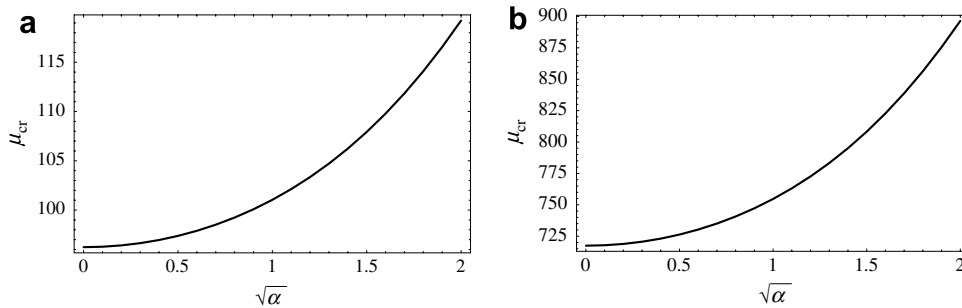


Fig. 4. For $\beta = 0$, μ_{cr} versus $\sqrt{\alpha} = g_0/h$. (a) $\varphi = 1$ and (b) $\varphi = 1/2$.

In Fig. 4, we plot for a square and a rectangular plate the variation of the critical Casimir force parameter μ_{cr} with the parameter $\sqrt{\alpha} = g_0/h$. It is clear that the linear plate theory predictions represented by the values ≈ 95 and ≈ 715 corresponding to $\alpha = 0$ lose accuracy with increasing g_0/h . Moreover, the absolute error in the linear plate theory prediction is enhanced with decreasing aspect ratio φ , as shown by the scales on the vertical axes in Fig. 4. These plots also reveal that Eq. (42) gives approximate values of μ_{cr} . For example, for $\alpha = 0$ and $\varphi = 1$, Eq. (42) gives $\mu_{cr} = 117.4$ as compared to 95 from Fig. 4.

5.1.1.2.2. *Nonzero prestress.* Recalling that the parameter β in Eq. (10) is a measure of the prestress, we plot in Fig. 5 the variation with β of the critical Casimir force parameter μ_{cr} for a square plate and a rectangular plate with $\varphi = 1/2$, and for $\alpha = 1$ and 4. For each case studied μ_{cr} increases with a decrease in the magnitude of the compressive prestress and an increase in the tensile prestress. Thus the safely fabricated device size can be modified by changing the prestress. We note that results depicted in Fig. 5 are in qualitative agreement with

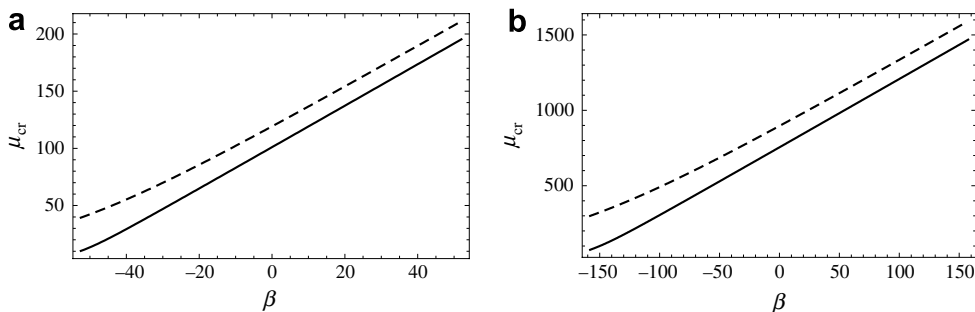


Fig. 5. For $\alpha = 1$ (solid line) and $\alpha = 4$ (dashed line), variation with β of the critical Casimir force parameter μ_{cr} for (a) square plate and (b) rectangular plate with $\varphi = 1/2$.

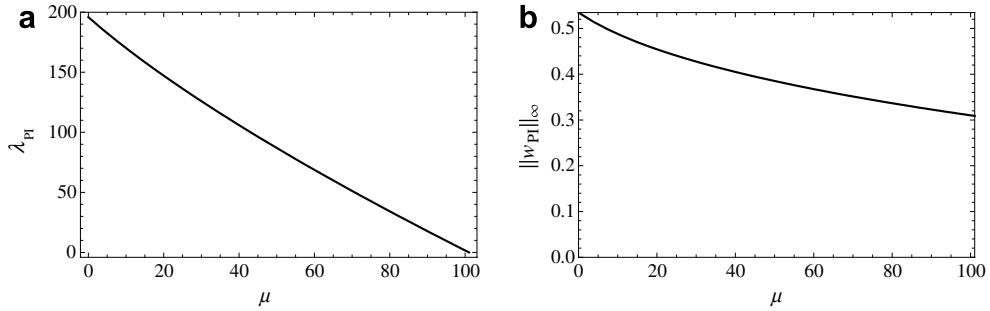


Fig. 6. (a) λ_{PI} and (b) $\|w_{PI}\|_{\infty}$ versus μ for a square plate with $\alpha = 1$ and $\beta = 0$.

those for a clamped–clamped MEM beam computed both with ANSYS using three-dimensional formulation of the problem, and with the one degree of freedom model of the beam, see Batra et al. (2006c).

5.1.1.3. Pull-in parameters for a fixed value of μ .

5.1.1.3.1. Zero prestress. In Figs. 6 and 7, we plot for a square and a rectangular plate the pull-in parameters versus μ in the range $[0, \mu_{cr}]$ for $\alpha = 1$ (that is, $g_0/h = 1$), $\beta = 0$ (that is, $\sigma_0 = 0$). As μ increases the pull-in parameter λ_{PI} decreases monotonically from its maximum value λ_{PI}^{max} corresponding to $\mu = 0$ to its minimum value 0 for $\mu = \mu_{cr}$; $\mu = \mu_{cr}$ represents the intersection of the curves with the horizontal axis. With an increase in μ the nondimensional maximum transverse displacement decreases monotonically from its maximum value $\|w_{PI}\|_{\infty}^{max}$ for $\mu = 0$ to its minimum value at $\mu = \mu_{cr}$.

For a MEMS made of a specified material, Eq. (10)₅ implies that $\ell^4/(h^3 g_0^5)$ is proportional to μ_{cr} . Thus μ_{cr} determines the device size that can be safely fabricated. This means that reduced–deflection ranges are allowable for devices having a large value of μ_{cr} since μ_{cr} is inversely proportional to g_0^5 . By comparing results depicted in Figs. 6 and 7, we conclude that a change in the aspect ratio of a plate from 1 to 1/2 significantly increases λ_{PI}^{max} , and it does not noticeably affect the difference $\|w_{PI}\|_{\infty}^{max} - \|w_{cr}\|_{\infty}$.

For $\mu = 0.3\mu_{cr}$ and $\alpha = 4$, we have plotted in Fig. 8 the deformed shapes of the square plate when $\lambda \simeq 180$ and $\|w\|_{\infty} \simeq 0.52$, and of the rectangular plate with $\varphi = 1/2$ when $\lambda \simeq 1300$ and $\|w\|_{\infty} \simeq 0.52$. Fringe plots of the Casimir pressure (cf. Eq. (6)) are also exhibited. In the undeformed plate grid lines were uniformly spaced. Thus by comparing the lengths of the curve segments between two consecutive curves with their original lengths one can estimate stretches at different points of the plate. For the same value of $\|w\|_{\infty}$ the maximum magnitude of the Casimir pressure for the rectangular plate is nearly an order of magnitude higher than that for the square plate; note that F_C in Eq. (6) does not depend upon the applied voltage. Its value is negative because it acts along the negative z -axis.

5.1.1.3.2. Nonzero prestress. In the absence of the Casimir force (that is, $\mu = 0$) Fig. 9 exhibits the variation with the prestress parameter β of the pull-in voltage λ_{PI} for a square plate and a rectangular plate with $\varphi = 1/2$, and also for $\alpha = 1$ and 4. In each case the pull-in voltage parameter increases nearly linearly with

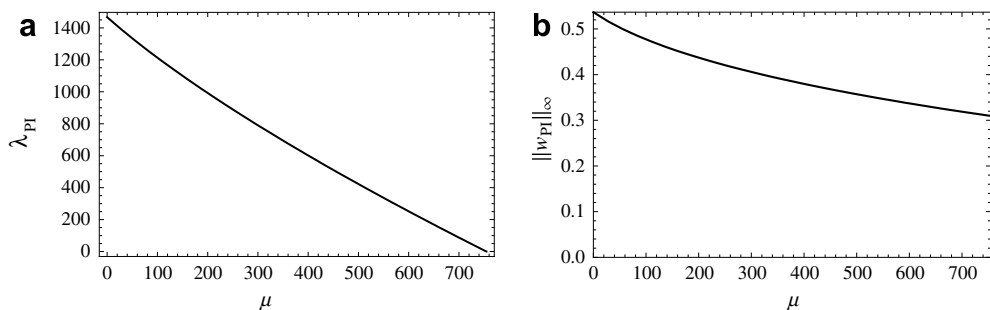


Fig. 7. (a) λ_{PI} and (b) $\|w_{PI}\|_{\infty}$ versus μ for a rectangular plate ($\varphi = 1/2$) with $\alpha = 1$ and $\beta = 0$.

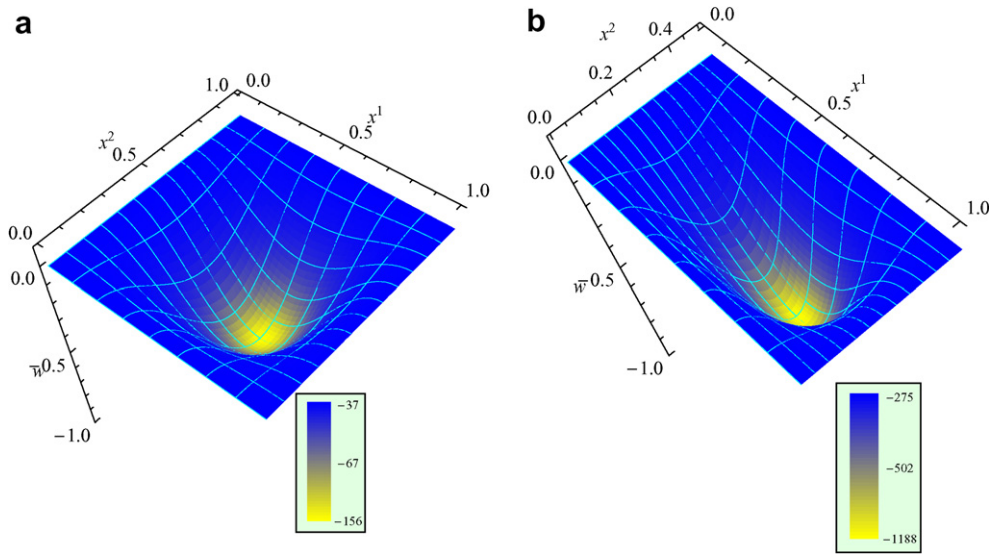


Fig. 8. For $\mu \simeq 0.3\mu_{cr}$ and $\alpha = 4$, deformed shape of (a) the square plate with $\lambda \simeq 180$ and $\|w\|_\infty \simeq 0.52$, and (b) rectangular plate with $\varphi = 1/2$, $\lambda \simeq 1300$ and $\|w\|_\infty \simeq 0.52$. Fringe plots of the Casimir pressure are also displayed.

an increase in β . We note that magnitudes of the initial compressive and tensile prestresses are limited, respectively, by the buckling instability of the MEMS and the tensile strength of the material of the MEMS.

5.1.2. Frequencies of a deformed plate

In Fig. 10, we have plotted for a square and a rectangular plate the fundamental natural frequency ω_0 of the deflected microplate versus λ for $\alpha = 4$, $\beta = 0$ (that is, no initial stress) and two different values of μ . The eigenfrequency is normalized with respect to the value $\bar{\omega}_0$ corresponding to $\lambda = 0$; nondimensional values of $\bar{\omega}_0$ for Figs. 10 and 11 are reported in Table 4. The corresponding dimensional values equal $\bar{\omega}_0 \sqrt{D/(\rho \ell^4)}$. The trend is nonmonotonic due to the combined effect of the strain hardening represented by $\alpha \mathbf{k}_3(\zeta)$ and the softening effect introduced by the Coulomb and the Casimir forces. Indeed, from Eq. (28) it is clear that the overall behavior of the Coulomb and the Casimir forces is equivalent to a nonlinear spring with negative spring constant. When the strain hardening effect is negligible the fundamental frequency monotonically decreases to zero, as is typically predicted by the linear plate theory.

We note that the presently computed non-dimensional fundamental frequencies of 36.1 and 98.6 match well with the 36.108 and 98.592 for square and rectangular plates reported by Arenas (2003).

Results in Fig. 11 show that for $\alpha = 1$ and $\beta = 0$ the fundamental frequency monotonically decreases, meaning that in this case the softening effect related to the Coulomb and the Casimir forces overwhelms

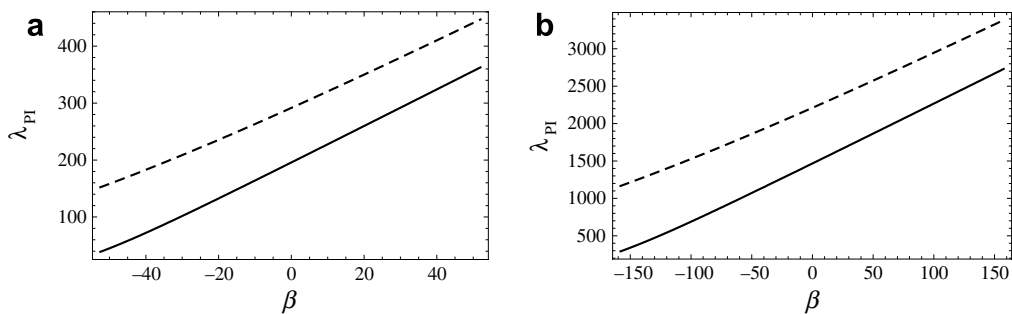


Fig. 9. For $\alpha = 1$ (solid line), $\alpha = 4$ (dashed line), and $\mu = 0$, variation with β of the pull-in voltage parameter λ_{PI} for (a) square plate and (b) rectangular plate with $\varphi = 1/2$.

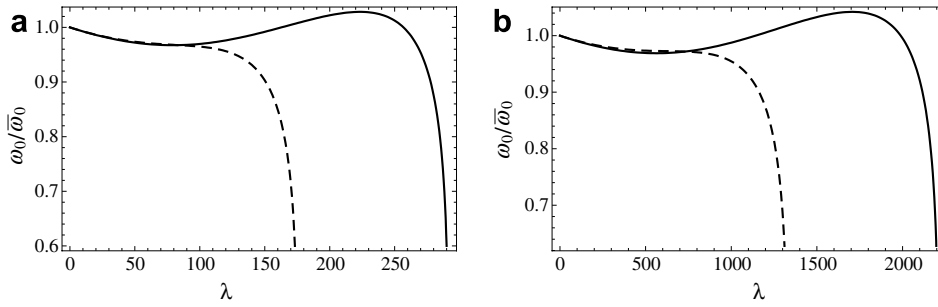


Fig. 10. Normalized fundamental natural frequency versus λ for $\mu = 0$ (solid line), $\mu \simeq 0.3\mu_{cr}$ (dashed line), $\alpha = 4$ and $\beta = 0$; (a) $\varphi = 1$ and (b) $\varphi = 1/2$.

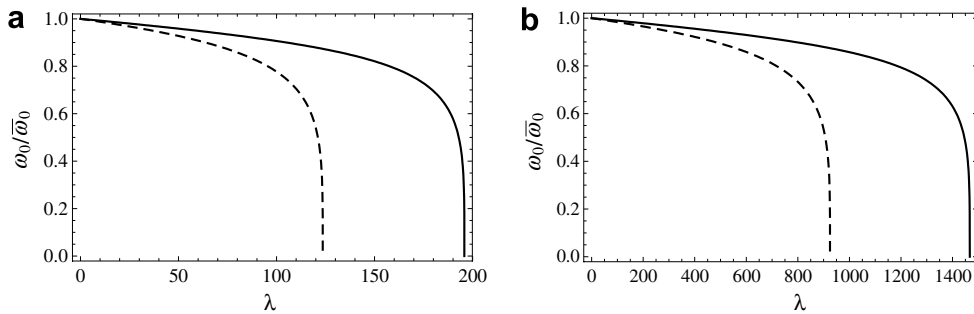


Fig. 11. Fundamental natural frequency versus λ for $\mu = 0$ (solid line), $\mu \simeq 0.3\mu_{cr}$ (dashed line), $\alpha = 1$ and $\beta = 0$; (a) $\varphi = 1$ and (b) $\varphi = 1/2$.

Table 4
Values of $\bar{\omega}_0$ in Figs. 10 and 11

α	$\varphi = 1$		$\varphi = 1/2$	
	$\mu = 0$	$\mu \simeq 0.3\mu_{cr}$	$\mu = 0$	$\mu \simeq 0.3\mu_{cr}$
1	36.1	34.1	98.6	93.0
4	36.1	33.9	98.6	92.7

the strain hardening effect. Note that λ corresponding to $\omega_0 = 0$ agrees with the λ_{PI} from Fig. 6 which of course should be true since in both cases $\det \mathbf{K}(\zeta, \alpha, \beta, \lambda, \mu) = 0$. This provides an alternative way to find the pull-in parameters.

5.1.3. Pull-in parameters for a membrane

For a linear elastic membrane the equation

$$-\Delta w + \frac{\lambda}{\beta(1+w)^2} + \frac{\mu}{\beta(1+w)^4} = 0 \tag{44}$$

governing static deflection under the action of the Coulomb and the Casimir forces is derived from Eq. (9a) with $\beta \gg 1$ and $\alpha/\beta \ll 1$. Since typically $E/\sigma_0 \sim 10^3$, we have $\ell^2 \gg h^2$ and $\ell^2 \gg g_0^2$. Therefore, the MEMS device experiences small deflections and the bending stiffness is negligible as compared to the in-plane stiffness due to a constant prestress in carrying the external load. Eq. (44) shows that μ_{cr} varies linearly with β or, equivalently, that the ratio μ_{cr}/β is constant. The same remark applies to λ_{PI}/β for a given $\mu \in [0, \mu_{cr}]$. A reduced-order model for the linear membrane can be derived from Eq. (25) by setting $\mathbf{k}_1 = \mathbf{k}_3 = \mathbf{0}$, and by

computing \mathbf{m} , \mathbf{k}_2 , \mathbf{f}_e , and \mathbf{f}_C in Eqs. (26a), (26b), and (26d) with the following basis functions for the transverse displacement:

$$\bar{w}_n^m(x^1, x^2) = \sin(n\pi x^1) \sin\left(\frac{n\pi x^2}{\varphi}\right). \tag{45}$$

Pull-in parameters λ_{PI}/β and $\|w_{PI}\|_\infty$ versus $\mu/\beta \in [0, \mu_{cr}/\beta]$ are plotted in Fig. 12 for a clamped square micromembrane by taking $n = 1$ in Eq. (45), implying that we use a 1 d.o.f. model.

5.2. Circular plate

We consider a circular plate of radius 1. The two-dimensional region corresponding to plate’s mid-surface is described by polar coordinates (x^1, x^2) , where x^1 and x^2 are the radial and the angular coordinates, respectively.

Integrals appearing in the reduced-order model for the microplate have been computed using the Gauss quadrature rule by placing 21×21 quadrature points in the region $[0, 1] \times [0, 2\pi]$. For the DIPIE algorithm we adopt $(\bar{x}^1, \bar{x}^2) = (0, 0)$ as the point whose displacement s is imposed.

The solution of the eigenvalue problem (14) with the method explained in Section 3.1 gives the following linearly independent basis functions for the in-plane displacement:

$$\bar{\mathbf{u}}_p(x^1, x^2) = A_{mn}^1 \frac{\partial \mathbf{J}_m}{\partial x^1}(\kappa'_{mn} x^1) \cos(mx^2) (\mathbf{g}^1 + x^1 \mathbf{g}^2), \tag{46a}$$

$$\bar{\mathbf{u}}_{(\bar{p}+1)\bar{q}+p}(x^1, x^2) = A_{mn}^2 \frac{\partial \mathbf{J}_m}{\partial x^1}(\kappa'_{mn} x^1) \sin(mx^2) (\mathbf{g}^1 + x^1 \mathbf{g}^2), \tag{46b}$$

$$\bar{\mathbf{u}}_{(2\bar{p}+1)\bar{q}+p}(x^1, x^2) = A_{mn}^3 m \mathbf{J}_m(\kappa_{mn} x^1) \cos(mx^2) \left(-\frac{\mathbf{g}^1}{x^1} + \mathbf{g}^2\right), \tag{46c}$$

$$\bar{\mathbf{u}}_{(3\bar{p}+1)\bar{q}+p}(x^1, x^2) = A_{mn}^4 m \mathbf{J}_m(\kappa_{mn} x^1) \sin(mx^2) \left(\frac{\mathbf{g}^1}{x^1} - \mathbf{g}^2\right), \tag{46d}$$

where

$$p = m\bar{q} + n, \quad m = 0, \dots, \bar{p}, \quad n = 1, \dots, \bar{q}.$$

Therefore, the number of nonzero basis functions for the in-plane displacement in Eq. (13b) is $P = \bar{q}(1 + 4\bar{p})$. In Eqs. (46), \mathbf{J}_m is a Bessel function of the first kind, and nondimensional variables κ'_{mn} and κ_{mn} are determined, respectively, as the n th roots of the following characteristic equations:

$$\left. \frac{\partial \mathbf{J}_m}{\partial x^1}(\kappa' x^1) \right|_{x^1=0} = 0, \quad \mathbf{J}_m(\kappa) = 0. \tag{47}$$

As basis functions for the transverse displacement we use the following family of axisymmetric functions, see for example Meirovitch (1967)

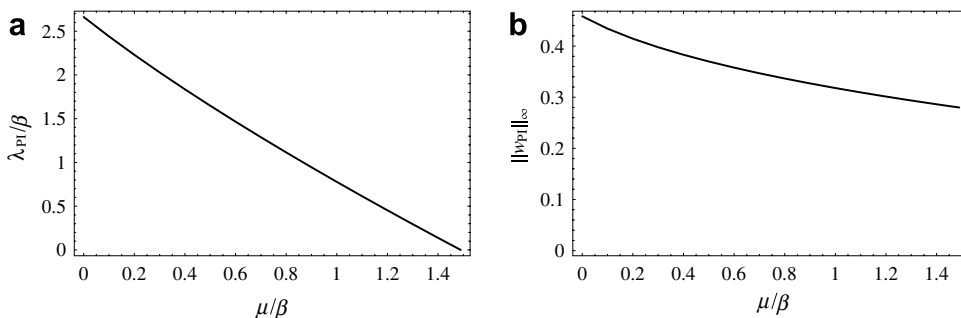


Fig. 12. For a clamped square membrane, pull-in parameters versus the Casimir force parameter.

$$\bar{w}_n(x^1) = A_n \left(\frac{J_0(\Lambda_n x^1)}{J_0(\Lambda_n)} - \frac{I_0(\Lambda_n x^1)}{I_0(\Lambda_n)} \right), \quad n = 1, \dots, N, \tag{48}$$

where I_0 is the modified Bessel function of the first kind, and nondimensional frequencies Λ_n are determined as roots of the equation

$$J_0(\Lambda)I_1(\Lambda) + J_1(\Lambda)I_0(\Lambda) = 0. \tag{49}$$

Because of the assumption of axisymmetry embodied in Eq. (48), a nonaxisymmetric solution (if there is one) will not be found. For annular micromembranes, nonaxisymmetric unstable equilibrium solutions exist after pull-in, see Pelesko et al. (2003), Batra et al. (2006a), Batra et al. (2007a). Plaut (2008) has also studied wrinkling instabilities in electrostatically loaded annular membranes.

Since the basis functions in Eq. (48) are axisymmetric, only in-plane modes that are also axisymmetric give nonzero entries of the matrix \mathbf{H}_p in Eq. (21). Therefore, results are computed with $\bar{p} = 0$ in Eq. (46), and the number of basis functions for the in-plane displacement equals $P = \bar{q}$.

5.2.1. Pull-in parameters from the static analysis

5.2.1.1. Comparison of results. Table 5 lists pull-in parameters $\|w_{PI}\|_\infty$ and λ_{PI} extracted for $\alpha = 1$, $\beta = 0$ and $\mu = 0$ and different values of \bar{q} and N in Eqs. (46) and (48). For the same \bar{q} the difference between results obtained with $N = 1$ and $N = 5$ is $\approx 1\%$.

For $\alpha = 1/(12(1 - \nu^2))$ and $\beta = 0$ the converged pull-in parameters $\|w_{PI}\|_\infty = 0.469$ and $\lambda_{PI} = 13.8$ match well with the corresponding ones $\|w_{PI}\|_\infty \approx 0.47$ and $\lambda_{PI} \approx 14$ obtained from Fig. 2 of Vogl and Nayfeh (2005); the authors employed a reduced-order model for a von Kármán circular microplate formulated in terms of the transverse displacement and the Airy stress function.

5.2.1.2. Critical values of the Casimir force parameter.

5.2.1.2.1. Zero prestress. In Table 6, we give values of the critical Casimir force parameter μ_{cr} and the corresponding infinity norm of the pull-in displacement $\|w_{cr}\|_\infty$ for $\alpha = 1$. As for results reported in Table 5, for the same \bar{q} the difference between values of pull-in parameters obtained with $N = 1$ and $N = 5$ is $\approx 1\%$.

Based on values listed in Tables 5 and 6 we use $\bar{q} = 2$ and $N = 1$ in Eqs. (46) and (48) for results presented below. Hence the reduced-order model has 3 basis functions and 1 degree of freedom.

The variation of the critical Casimir force parameter μ_{cr} with the parameter $\sqrt{\alpha} = g_0/h$ is plotted in Fig. 13. For $g_0/h = 2$ the value 7.2 of μ_{cr} computed with the linear plate theory (corresponding to $\alpha = 0$) has an error of $\approx 16\%$.

5.2.1.2.2. Nonzero prestress. For $\alpha = 1$ and 4 Fig. 14 depicts the variation of the critical Casimir force parameter μ_{cr} with the prestress parameter β . As the prestress parameter β is increased from -15 to 30 , μ_{cr} increases almost linearly.

5.2.1.3. Pull-in parameters for a fixed value of μ .

5.2.1.3.1. Zero prestress. Pull-in parameters versus μ in the range $[0, \mu_{cr}]$ for $\alpha = 1$, $\beta = 0$ are plotted in Fig. 15. As μ increases pull-in parameters decrease monotonically from their maximum values corresponding to $\mu = 0$ to their minimum values for $\mu \approx 8$. For $\mu = \mu_{cr}$, $\lambda = 0$ and the device collapses with zero applied voltage.

Table 5

Nondimensional pull-in parameters $\|w_{PI}\|_\infty$ and λ_{PI} for different number of basis functions to approximate the in-plane and the transverse displacements

N	$\ w_{PI}\ _\infty$			λ_{PI}		
	\bar{q}			\bar{q}		
	1	2	4	1	2	4
1	0.542	0.528	0.528	16.2	15.7	15.7
3	0.535	0.522	0.522	16.2	15.7	15.7
5	0.534	0.522	0.522	16.2	15.7	15.7

Table 6

Critical force parameter μ_{cr} and the corresponding pull-in displacement infinity norm $\|w_{cr}\|_{\infty}$ with different number of basis functions for the in-plane and the transverse displacements

N	$\ w_{cr}\ _{\infty}$			μ_{cr}		
	\bar{q}			\bar{q}		
	1	2	4	1	2	4
1	0.310	0.305	0.305	8.22	8.12	8.12
3	0.307	0.302	0.302	8.24	8.14	8.14
5	0.306	0.302	0.301	8.24	8.14	8.14

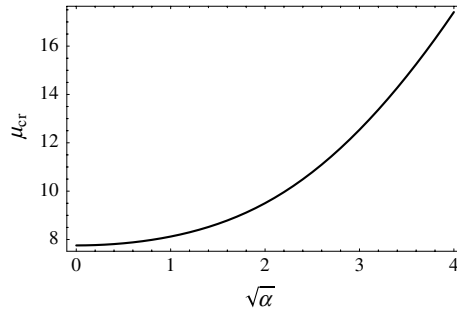


Fig. 13. For $\beta = 0$, μ_{cr} versus $\sqrt{\alpha} = g_0/h$.

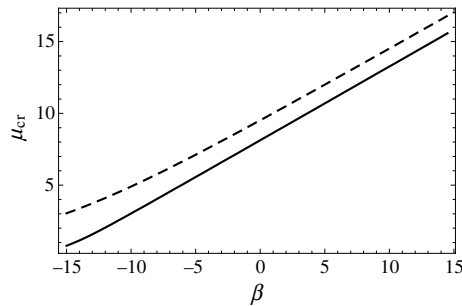


Fig. 14. Variation with β of the critical Casimir force parameter μ_{cr} for the circular plate with $\alpha = 1$ (solid line) and $\alpha = 4$ (dashed line).

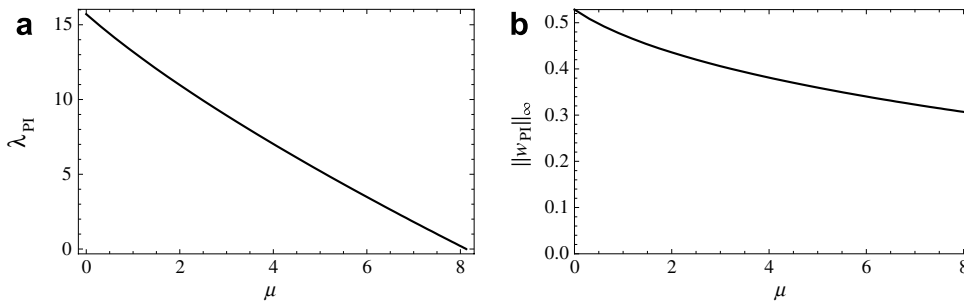


Fig. 15. (a) λ_{PI} and (b) $\|w_{PI}\|_{\infty}$ versus μ for a circular plate with $\alpha = 1$ and $\beta = 0$.

For $\mu \simeq 0.3\mu_{cr}$ and $\alpha = 4$ the deformed shape of the circular plate when $\lambda \simeq 14$ and $\|w\|_{\infty} \simeq 0.5$ is shown in Fig. 16. Fringe plots of the Casimir pressure (cf. Eq. (6)) are superimposed on the deformed plate.

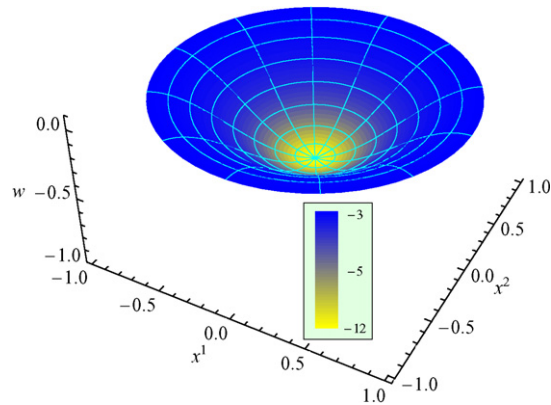


Fig. 16. For $\mu \simeq 0.3\mu_{cr}$ and $\alpha = 4$, the deformed shape of the circular plate with $\lambda \simeq 14$ and $\|w\|_\infty \simeq 0.5$. Fringe plots of the Casimir pressure are also displayed.

5.2.1.3.2. *Nonzero prestress.* For $\mu = 0$, and $\alpha = 1$ and 4 , the variation with β of the pull-in voltage λ_{PI} is plotted in Fig. 17. For both values of α , the variation of λ_{PI} with β is essentially linear.

5.2.2. *Frequencies of a deformed plate*

In Fig. 18, we plot the fundamental natural frequency ω_0 of the deflected microplate versus λ for $\beta = 0$ and different values of α and μ . The eigenfrequency is normalized with respect to the value $\bar{\omega}_0$ corresponding to $\lambda = 0$; nondimensional values of $\bar{\omega}_0$ for Fig. 18 are reported in Table 7. The corresponding dimensional values

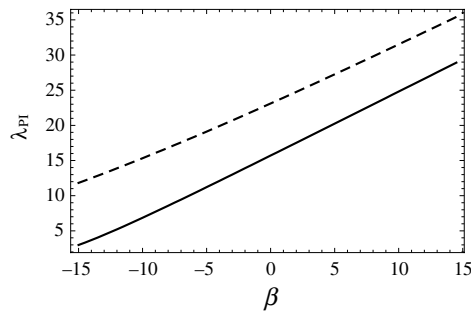


Fig. 17. For $\mu = 0$, variation with β of the pull-in voltage parameter λ_{PI} for the circular plate with $\alpha = 1$ (solid line) and $\alpha = 4$ (dashed line).

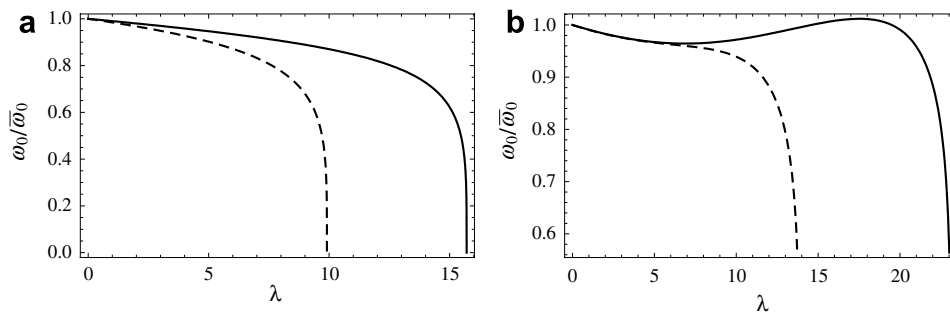


Fig. 18. Normalized fundamental natural frequency versus λ for $\mu = 0$ (solid line), $\mu \simeq 0.3\mu_{cr}$ (dashed line), and $\beta = 0$; (a) $\alpha = 1$ and (b) $\alpha = 4$.

Table 7
For the circular plate, values of $\bar{\omega}_0$ in Fig. 18

α	$\mu = 0$	$\mu \simeq 0.3\mu_{cr}$
1	10.2	9.64
4	10.2	9.59

equal $\bar{\omega}_0 \sqrt{D/(\rho \ell^4)}$. With increasing μ and decreasing α the nonmonotonic behavior decreases due to the increased softening effect introduced by the Casimir force. As for the rectangular plate, for $\mu = 0$ and $\alpha = 1$ the value $\lambda_{PI} \approx 15$ agrees with that obtained in Fig. 15 by the DIPIE algorithm.

5.2.3. Pull-in parameters for a membrane

We plot in Fig. 19 pull-in parameters of a circular clamped membrane obtained by solving the reduced-order model derived from Eq. (44) by using the following basis functions for the transverse displacement

$$\bar{w}_n^m(x^1) = J_0(\kappa_{0n}x^1), \tag{50}$$

and $n = 1$. They match very well with those obtained by Batra et al. (2007a), Batra et al. (2006a) by solving the two-dimensional governing equation with the meshless local Petrov-Galerkin method (Atluri and Shen, 2002). For $\mu = 0$, the nondimensional pull-in voltage and the pull-in maximum displacement computed with the one degree-of-freedom model equal 0.783 and 0.456, while those predicted by the MLPG method in Batra et al. (2006a) equal 0.791 and 0.443, respectively.

5.3. Detachment dimensions

The maximum size of the MEM plates that does not stick with the substrate without the application of voltage is called the detachment dimension (Lin and Zhao, 2005). For a given initial gap g_0 the detachment size can be found from Eq. (10)₅ by setting $\mu = \mu_{cr}$. Using values of μ_{cr} listed in Tables 2, 3, and 6 for the square, rectangular and circular plates, respectively, we get their maximum sizes that can be safely fabricated. For $h = 1 \mu\text{m}$, $g_0 = h$, $\sigma_0 = 0$, $E = 169 \text{ GPa}$, $\nu = 0.25$ the detachment sizes of various plates are summarized in Table 8.

In terms of the area A of the MEM plate, $\ell \propto \sqrt{A}$, $\sqrt{A/\varphi}$, and $\sqrt{4A/\pi}$ for the square, the rectangular and the circular plates. Thus if A , the plate thickness h and the initial gap g_0 are kept constant, then the maximum dimensions listed in Table 8 for the rectangular and the circular plates will decrease by factors of $\sqrt{\varphi}$ and $2/\sqrt{\pi}$, respectively. If the device length is kept fixed then μ_{cr} gives the minimum value of the gap g_0 .

5.4. Remarks

In Batra et al. (2008b) we showed that the 1 degree-of-freedom model for a narrow MEM beam derived by using an approach similar to that adopted here gave values of pull-in parameters that differed by 5%

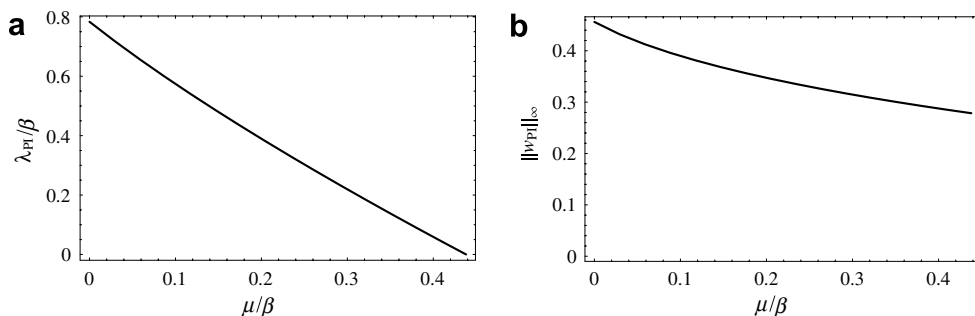


Fig. 19. For a clamped circular membrane, pull-in parameters versus the Casimir force parameter.

Table 8

Maximum sizes of square, rectangular ($\varphi = 1/2$) and circular microplates that can be safely fabricated for $h = 1 \mu\text{m}$

Size (μm)	Plate		
	Square (side)	Rectangular (longer side)	Circular (radius)
	3692	6103	1966

from the values derived from the analysis of the coupled three-dimensional electromechanical problem with the commercial code ANSYS using nearly 1400 degrees of freedom. For the circular MEM membranes, the 1 d.o.f. model of Section 5.2.3 gives pull-in parameters that differ by about 3% from the numerical solution of the nonlinear governing equations using 86 degrees of freedom for a quarter of the circular membrane. These comparisons provide robustness and accuracy of the proposed reduced-order models. In the absence of a solution of the nonlinear partial differential Eqs. (9a) and (9b) with inertia forces neglected and under the appropriate boundary conditions, the error in the converged solution obtained herein can not be ascertained. A comparison of the solution of Eqs. (9a) and (9b) with that of equations governing three-dimensional deformations of the MEM plate will provide information about the adequacy of the plate model adopted here. Of course, an ultimate test of the adequacy of a mathematical model lies in its ability to predict results that agree well with the experimental observations.

We note that the work has been extended to MEM elliptic plates by Batra et al. (2008a).

6. Conclusions

We have presented a unified approach to derive reduced-order models for clamped rectangular and circular microelectromechanical von Kármán plates subject to both the Coulomb and the Casimir forces. The nonlinear governing equations for the three displacement components are coupled. Mode shapes of a linear elastic plate are taken as the basis functions for the transverse displacement. The in-plane displacement is expressed as the sum of the displacement vectors for the longitudinal and the transverse waves. For the geometries considered, basis functions for the in-plane displacements can be found analytically. For other geometries, these basis functions may be computed numerically.

The pull-in voltage and the pull-in deflection extracted from these reduced-order models for rectangular and circular plates agree well with those available in the literature. Free vibrations of a plate predeformed by the applied voltage and the Casimir force are analyzed; the voltage for which the first natural frequency equals zero gives the pull-in voltage. It is found that 9 basis functions for the rectangular plate and a 3 basis functions for the circular plate give converged values of the pull-in parameters which agree well with those reported in the literature. Also, the models using 3 basis functions for the rectangular plate and 2 basis functions for the circular plate give pull-in parameters with less than 4% error.

The reduced-order model for a plate is simplified to that for the corresponding membrane by neglecting the bending stiffness of the plate. Pull-in parameters for the rectangular and the circular membranes from the 1 degree-of-freedom reduced-order models are found to agree well with those obtained by solving numerically the complete set of governing nonlinear partial differential equations.

Critical values of the Casimir force parameter for these plates are also determined. These give sizes of microelectromechanical systems that can be safely fabricated. The analysis is valid for separation distances between the two plates $\gtrsim 1 \mu\text{m}$, for which the geometric interaction between perfectly conducting plates is given by Eq. (6).

Appendix A. Identities used in the derivation of the reduced-order model

Let $f : \Omega \rightarrow \mathbb{R}$, $\mathbf{f}, \mathbf{g} : \Omega \rightarrow \mathbb{V}$, and $\mathbf{F}, \mathbf{G} : \Omega \rightarrow \mathbb{T}$ be a scalar, vector, and second order tensor fields in Ω . We denote the inner product between two vectors as $\mathbf{a} \cdot \mathbf{b}$; the space \mathbb{T} has the natural inner product, see for example Batra (2005), defined by $\mathbf{F} \cdot \mathbf{G} = \text{tr}(\mathbf{F}\mathbf{G}^T) = \sum_{i,j} F_{ij}G_{ij}$.

The tensor product \otimes between two vectors \mathbf{f} and \mathbf{g} is the second order tensor that assigns to each vector \mathbf{a} the vector $(\mathbf{g} \cdot \mathbf{a})\mathbf{f}$:

$$(\mathbf{f} \otimes \mathbf{g})\mathbf{a} = (\mathbf{g} \cdot \mathbf{a})\mathbf{f}. \quad (\text{A.1})$$

Then the following rules apply

$$\mathbf{F}(\mathbf{f} \otimes \mathbf{g}) = (\mathbf{F}\mathbf{f}) \otimes \mathbf{g}, \quad (\mathbf{f} \otimes \mathbf{g})\mathbf{F} = \mathbf{f} \otimes (\mathbf{F}^T\mathbf{g}), \quad (\text{A.2})$$

$$\text{tr}(\mathbf{f} \otimes \mathbf{g}) = \mathbf{f} \cdot \mathbf{g}, \quad (\text{A.3})$$

$$(\mathbf{f} \otimes \mathbf{g})^T = \mathbf{g} \otimes \mathbf{f}. \quad (\text{A.4})$$

Moreover, the following identities hold, see for example Gurtin (1981):

$$\text{div}(\nabla^T\mathbf{f}) = \nabla\text{div}\mathbf{f}, \quad (\text{A.5})$$

$$\text{div}(f\mathbf{f}) = f\text{div}\mathbf{f} + \mathbf{f} \cdot \nabla f, \quad (\text{A.6})$$

$$\text{div}(\mathbf{F}^T\mathbf{f}) = \mathbf{f} \cdot \text{div}\mathbf{F} + \text{tr}(\mathbf{F}\nabla\mathbf{f}). \quad (\text{A.7})$$

Appendix B. Differentiation in curvilinear coordinates

For a comprehensive treatment of the material briefly outlined below, see Bowen and Wang (1976).

Let (x^1, x^2) be curvilinear coordinates related to rectangular Cartesian coordinates (z^1, z^2) by

$$z^1 = \hat{z}^1(x^1, x^2), \quad z^2 = \hat{z}^2(x^1, x^2), \quad (\text{B.1})$$

$$x^1 = \hat{x}^1(z^1, z^2), \quad x^2 = \hat{x}^2(z^1, z^2). \quad (\text{B.2})$$

Covariant and contravariant natural basis associated with the curvilinear coordinates are defined by

$$\mathbf{g}_i = \frac{\partial}{\partial x^i} (\hat{z}^1 \mathbf{i}_1 + \hat{z}^2 \mathbf{i}_2), \quad \mathbf{g}^i = \hat{\nabla} \hat{x}^i, \quad (\text{B.3})$$

where \mathbf{i}_j are basis vectors associated with the Cartesian coordinates, and $\hat{\nabla} = \frac{\partial}{\partial z^1} \mathbf{i}_1 + \frac{\partial}{\partial z^2} \mathbf{i}_2$. The covariant components g_{ij} and the contravariant components g^{ij} of the metric tensor are given, respectively, by $g_{ij} = \mathbf{g}_i \cdot \mathbf{g}_j$ and $g^{ij} = \mathbf{g}^i \cdot \mathbf{g}^j$. Since $\mathbf{g}^i \cdot \mathbf{g}_j = \delta_j^i$ where δ_j^i is the Kronecker delta, it follows that $[g^{ij}] = [g_{ij}]^{-1}$.

Let ϕ be a scalar field. The gradient $\nabla\phi$ of ϕ is the vector field given by

$$\nabla\phi = \frac{\partial\phi}{\partial x^j} \mathbf{g}^j = \phi_{,j} \mathbf{g}^j. \quad (\text{B.4})$$

Here and below, a repeated index appearing as a subscript and a superscript in the same term is summed over its range of values. Let ψ be a vector field. The gradient $\nabla\psi$ of ψ is the second order tensor field given by

$$\nabla\psi = \psi^i_{,j} \mathbf{g}_i \otimes \mathbf{g}^j = \psi_{,i,j} \mathbf{g}^i \otimes \mathbf{g}^j, \quad (\text{B.5})$$

where the derivatives $\psi^i_{,j}$ and $\psi_{,i,j}$ are defined by

$$\psi^i_{,j} = \frac{\partial\psi^i}{\partial x^j} + \left\{ \begin{matrix} i \\ jk \end{matrix} \right\} \psi^k, \quad (\text{B.6})$$

$$\psi_{,i,j} = \frac{\partial\psi_{,i}}{\partial x^j} - \left\{ \begin{matrix} k \\ ji \end{matrix} \right\} \psi_k, \quad (\text{B.7})$$

and $\left\{ \begin{matrix} i \\ jk \end{matrix} \right\}$ are the Christoffel symbols, given in the next subsection for polar coordinates. A convenient formula for computing Christoffel symbols is

$$\left\{ \begin{matrix} i \\ jk \end{matrix} \right\} = \frac{1}{2} g^{ih} \left(\frac{\partial g_{jh}}{\partial x^k} + \frac{\partial g_{kh}}{\partial x^j} - \frac{\partial g_{jk}}{\partial x^h} \right). \quad (\text{B.8})$$

Expression (B.7) is suitable for the calculation of $\nabla\nabla\phi$, since from Eq. (B.4) the components of $\nabla\phi$ are covariant.

Combining Eq. (B.5) with Eqs. (A.3) and (A.2) we obtain the following component representations of relations appearing in (21)

$$\text{tr}(\nabla\psi\nabla^T\psi) = g^{jk}g^{ih}\psi_{i,j}\psi_{h,k} = g^{jk}\psi_j^h\psi_{h,k}, \tag{B.9}$$

$$\text{div}\psi = \text{tr}\nabla\psi = \psi_{,i}^i = g^{ij}\psi_{i,j}, \tag{B.10}$$

$$\text{tr}(\nabla\phi \otimes \nabla^T\psi\nabla\phi) = \nabla^T\psi\nabla\phi \cdot \nabla\phi = \frac{\partial\phi}{\partial x^i}\psi_j^i g^{jk} \frac{\partial\phi}{\partial x^k}. \tag{B.11}$$

Let $(\mathbf{g}_1, \mathbf{g}_2, \mathbf{g}_3)$ be an orthogonal basis of a three-dimensional Euclidean space \mathbb{E} . The curl of the vector field Ψ is the vector field defined by, see for example Bowen and Wang (1976):

$$\text{curl}\Psi = -\frac{e^{ijk}}{\sqrt{g}} \frac{\partial\Psi_j}{\partial x^k} \mathbf{g}_i, \tag{B.12}$$

where $g = \det[g_{ij}]$, and $e^{ijk} = 0$ if any of the two indices are equal, $e^{ijk} = \pm 1$ if $\{i, j, k\}$ is an even or an odd permutation of $\{1, 2, 3\}$, respectively.

In the special case when Ψ is a field on a two-dimensional region Ω with unit normal vector field \mathbf{g}_3 , the expression for the curl simplifies to

$$\text{curl}\Psi = \frac{1}{\sqrt{g}} \left(-\frac{\partial\Psi_3}{\partial x^2} \mathbf{g}_1 + \frac{\partial\Psi_3}{\partial x^1} \mathbf{g}_2 + \left(\frac{\partial\Psi_2}{\partial x^1} - \frac{\partial\Psi_1}{\partial x^2} \right) \mathbf{g}_3 \right). \tag{B.13}$$

B.1. Polar coordinates

Let $x^1 \in [0, R]$ and $x^2 \in [0, 2\pi]$ be polar coordinates. They are related to rectangular Cartesian coordinates (z^1, z^2) by

$$z^1 = x^1 \cos x^2, \quad z^2 = x^1 \sin x^2. \tag{B.14}$$

The covariant components of the metric tensor are

$$[g_{ij}] = \begin{bmatrix} 1 & 0 \\ 0 & (x^1)^2 \end{bmatrix}. \tag{B.15}$$

According to Eq. (B.8), in polar coordinates the nonzero Christoffel symbols are

$$\left\{ \begin{matrix} 1 \\ 22 \end{matrix} \right\} = -x^1, \quad \left\{ \begin{matrix} 2 \\ 12 \end{matrix} \right\} = \left\{ \begin{matrix} 2 \\ 21 \end{matrix} \right\} = \frac{1}{x^1}. \tag{B.16}$$

References

Abdel-Rahman, E.M., Younis, M.I., Nayfeh, A.H., 2002. Characterization of the mechanical behavior of an electrically actuated microbeam. *Journal of Micromechanics and Microengineering* 12 (6), 759–766.

Arenas, J.P., 2003. On the vibration analysis of rectangular clamped plates using the virtual work principle. *Journal of Sound and Vibration* 266 (4), 912–918.

Atluri, S.N., Shen, S., 2002. The meshless local Petrov-Galerkin (MLPG) method: a simple & less-costly alternative to the finite element and boundary element methods. *CMES: Computer Modeling in Engineering & Sciences* 3 (1), 11–51.

Bárceñas, J., Reyes, L., Esquivel-Sirvent, R., 2005. Scaling of micro- and nanodevices actuated by Casimir forces. *Applied Physics Letters* 87, 263106.

Batra, R.C., 2005. *Elements of Continuum Mechanics*. AIAA: American Institute of Aeronautics and Astronautics, Reston, VA.

Batra, R.C., Porfiri, M., Spinello, D., 2006a. Analysis of electrostatic MEMS using meshless local Petrov-Galerkin (MLPG) method. *Engineering Analysis with Boundary Elements* 30 (11), 949–962.

Batra, R.C., Porfiri, M., Spinello, D., 2006b. Capacitance estimate for electrostatically actuated narrow microbeams. *Micro & Nano Letters* 1 (2), 71–73.

Batra, R.C., Porfiri, M., Spinello, D., 2006c. Electromechanical model of electrically actuated narrow microbeams. *Journal of Microelectromechanical Systems* 15 (5), 1175–1189.

Batra, R.C., Porfiri, M., Spinello, D., 2007a. Effects of Casimir force on pull-in instability in micromembranes. *Europhysics Letters* 77, 20010.

- Batra, R.C., Porfiri, M., Spinello, D., 2007b. Review of modeling electrostatically actuated microelectromechanical systems. *Smart Materials and Structures* 16, R23–R31.
- Batra, R.C., Porfiri, M., Spinello, D., 2008a. Vibrations and pull-in instabilities of microelectromechanical von Kármán elliptic plates incorporating the Casimir force. *Journal of Sound and Vibration*, in press, doi:10.1016/j.jsv.2008.02.008.
- Batra, R.C., Porfiri, M., Spinello, D., 2008b. Vibrations of narrow microbeams predeformed by an electric field. *Journal of Sound and Vibration* 309 (3), 600–612.
- Batra, R.C., Porfiri, M., Spinello, D., 2008c. Effect of van der Waals force and thermal stress on pull-in instability of microplates. *Sensors* 8, 1048–1069.
- Bochobza-Degani, O., Elata, D., Nemirovsky, Y., 2002. An efficient DIPIE algorithm for CAD of electrostatically actuated MEMS devices. *Journal of Microelectromechanical Systems* 11 (5), 612–620.
- Bordag, M., 2006. Casimir effect for a sphere and a cylinder in front of a plane and corrections to the proximity force theorem. *Physical Review D* 73, 125018.
- Bordag, M., Mohideen, U., Mostepanenko, V.M., 2001. New developments in the Casimir effect. *Physics Reports* 353, 1–205.
- Bowen, R.M., Wang, C.-C., 1976. In: *Introduction to Vectors and Tensors*, vol. 2. Plenum Press, New York.
- Castañer, L.M., Senturia, S.D., 1999. Speed-energy optimization of electrostatic actuators based on pull-in. *Journal of Microelectromechanical Systems* 8 (3), 290–298.
- Chu, P.B., Nelson, P.R., Tachiki, M.L., Pister, K.S., 1996. Dynamics of polysilicon parallel-plate electrostatic actuators. *Sensors and Actuators A* 52, 216–220.
- Ding, J.-N., Wen, S.-Z., Meng, Y.-G., 2001. Theoretical study of the sticking of a membrane strip in MEMS under the Casimir effect. *Journal of Micromechanics and Microengineering* 11, 202–208.
- Francais, O., Dufour, I., 1999. Normalized abacus for the global behavior of diaphragms: pneumatic, electrostatic, piezoelectric or electromagnetic actuation. *Journal of Modeling and Simulation of Microsystems* 2, 149–160.
- Gies, H., Klingmüller, K., 2006. Casimir effect for curved geometries: Proximity-Force-Approximation validity limits. *Physical Review Letters* 96, 220401.
- Gupta, R.K., Senturia, S.D., January 1997. Pull-in time dynamics as a measure of absolute pressure. In: *Proceedings IEEE International Workshop on Microelectromechanical Systems (MEMS'97)*. Nagoya, Japan, pp. 290–294.
- Gurtin, M.E., 1981. *An Introduction to Continuum Mechanics*. Academic Press, Inc., San Diego, California.
- Hung, E.S., Senturia, S.D., 1999. Extending the travel range of analog-tuned electrostatic actuators. *Journal of Microelectromechanical Systems* 8 (4), 497–505.
- Israelachvili, J.N., 1991. *Intermolecular and Surface Forces*, second ed. Academic Press, London.
- Israelachvili, J.N., Tabor, D., 1972. The measurement of van der Waals dispersion forces in the range 1.5 to 130 nm. *Proceedings of the Royal Society of London, Series A* 331, 19–38.
- Klimchitskaya, G.L., Mohideen, U., Mostepanenko, V.M., 2000. Casimir and van der Waals forces between two plates or a sphere (lens) above a plate made of real metals. *Physical Review A* 61, 062107.
- Krylov, S., Maimon, R., 2004. Pull-in dynamics of an elastic beam actuated by continuously distributed electrostatic force. *Journal of Vibration and Acoustics* 126, 332–342.
- Kuang, J.-H., Chen, C.-J., 2004. Dynamic characteristics of shaped micro-actuators solved using the differential quadrature method. *Journal of Micromechanics and Microengineering* 14 (4), 647–655.
- Laliotis, A., Maurin, I., Todorov, P., Hamdi, I., Dutier, G., Yarovitski, A., Saltiel, S., Gorza, M.-P., Fichet, M., Ducloy, M., Bloch, D., March 2007. Testing the distance-dependence of the van der Waals interaction between an atom and a surface through spectroscopy in a vapor nanocell. In: *Atanasov, P.A., Dreischuh, T.N., Gateva, S.V., Kovachev, L.M. (Eds.), Proceedings of SPIE 14th International School on Quantum Electronics: Laser Physics and Applications, Peter A. Atanasov, Tanja N. Dreischuh, Sanka V. Gateva, Lubomir M. Kovachev, (Eds.), vol. 6604, 660406*.
- Lamoreaux, S.K., 2005. The Casimir force: background, experiments, and applications. *Reports on Progress in Physics* 68, 201–236.
- Landau, L.D., Lifshitz, E.M., 1986. *Theory of Elasticity*. Pergamon Press, New York.
- Lifshitz, E.M., 1956. The theory of molecular attractive forces between solids. *Soviet Physics JETP* 2, 73–83.
- Lin, W.-H., Zhao, Y.-P., 2005. Casimir effect on the pull-in parameters of nanometer switches. *Microsystem Technologies* 11 (2), 80–85.
- Lin, W.-H., Zhao, Y.-P., 2007. Influence of damping on the dynamical behavior of the electrostatic parallel-plate and torsional actuators with intermolecular forces. *Sensors* 7, 3012–3026.
- Mansfield, E.H., 1989. *The Bending & Stretching of Plates*, second ed. Cambridge University Press, Cambridge, New York (Chapter 9).
- Meirovitch, L., 1967. *Analytical Methods in Vibrations*. Macmillan, New York.
- Nathanson, H.C., Newell, W.E., Wickstrom, R.A., Davis, J.R., 1967. The resonant gate transistor. *IEEE Transactions on Electron Devices* 14 (3), 117–133.
- Nayfeh, A.H., Younis, M.I., 2005. Dynamics of MEMS resonators under superharmonic and subharmonic excitations. *Journal of Micromechanics and Microengineering* 15, 1840–1847.
- Ng, T.Y., Jiang, T.Y., Lam, K.Y., Reddy, J.N., 2004. A coupled field study on the non-linear dynamic characteristics of an electrostatic micropump. *Journal of Sound and Vibration* 273, 989–1006.
- Nguyen, C.T.C., Katehi, L.P.B., Rebeiz, G.M., 1998. Micromachined devices for wireless communications. In: *Proceedings of the IEEE*, vol. 86, pp. 1756–1768.
- Pamidighantam, S., Puers, R., Baert, K., Tilmans, H.A.C., 2002. Pull-in voltage analysis of electrostatically actuated beam structures with fixed-fixed and fixed-free end conditions. *Journal of Micromechanics and Microengineering* 12 (4), 458–464.
- Pelesko, J., Triolo, A., 2001. Nonlocal problems in MEMS device control. *Journal of Engineering Mathematics* 41 (4), 345–366.

- Pelesko, J.A., 2002. Mathematical modeling of electrostatic MEMS with tailored dielectric properties. *SIAM Journal of Applied Mathematics* 62 (3), 888–908.
- Pelesko, J.A., Bernstein, D.H., 2002. *Modeling MEMS and NEMS*. Chapman & Hall, Boca Raton, Fla (Chapter 7).
- Pelesko, J.A., Bernstein, D.H., McCuan, J., February 2003. Symmetry and symmetry breaking in electrostatic MEMS. In: *Proceedings of Modeling and Simulation of Microsystems*. San Francisco, CA, USA, pp. 304–307.
- Pelesko, J.A., Chen, X.Y., 2003. Electrostatic deflections of circular elastic membranes. *Journal of Electrostatics* 57, 1–12.
- Porfiri, M., 2008. Vibrations of parallel arrays of electrostatically actuated microplates. *Journal of Sound and Vibration*, in press, doi:10.1016/j.jsv.2008.02.007.
- Rhoads, J.F., Shaw, S.W., Turner, K.L., 2006. The nonlinear response of resonant microbeam systems with purely-parametric electrostatic actuation. *Journal of Micromechanics and Microengineering* 16, 890–899.
- Serry, F.M., Walliser, D., Maclay, G.J., 1998. The role of the Casimir effect in the static deflection and stiction of membrane strips in microelectromechanical systems (MEMS). *Journal of Applied Physics* 84 (5), 2501–2506.
- Taylor, G.I., 1968. The coalescence of closely spaced drops when they are at different electric potentials. *Proceedings of the Royal Society A* 306, 423–434.
- Tilmans, H.A., Legtenberg, R., 1994a. Electrostatically driven vacuum-encapsulated polysilicon resonators: Part I. Design and fabrication. *Sensors and Actuators A* 45, 57–66.
- Tilmans, H.A., Legtenberg, R., 1994b. Electrostatically driven vacuum-encapsulated polysilicon resonators: Part II. Theory and performance. *Sensors and Actuators A* 45 (1), 67–84.
- Timoshenko, S., 1970. *Theory of Elasticity*, third ed. McGraw-Hill Companies, New York.
- Vogl, G.W., Nayfeh, A.H., 2005. A reduced-order model for electrically actuated clamped circular plates. *Journal of Micromechanics and Microengineering* 15, 684–690.
- Xie, W.C., Lee, H.P., Lim, S.P., 2003. Nonlinear dynamic analysis of MEMS switches by nonlinear modal analysis. *Nonlinear Dynamics* 31, 243–256.
- Younis, M.I., Abdel-Rahman, E.M., Nayfeh, A.H., 2003. A reduced-order model for electrically actuated microbeam-based MEMS. *Journal of Microelectromechanical Systems* 12 (5), 672–680.
- Younis, M.I., Nayfeh, A.H., 2003. A study of the nonlinear response of a resonant microbeam to an electric actuation. *Nonlinear Dynamics* 31, 91–117.
- Zhang, Y., Zhao, Y.-P., 2006. Numerical and analytical study on the pull-in instability of micro-structure under electrostatic loading. *Sensors and Actuators A: Physical* 127, 366–380.
- Zhao, X., Abdel-Rahman, E.M., Nayfeh, A.H., 2004. A reduced-order model for electrically actuated microplates. *Journal of Micromechanics and Microengineering* 14 (7), 900–906.
- Zhao, Y.-P., Wang, L.S., Yu, T.X., 2003. Mechanics of adhesion in MEMS—a review. *Journal of Adhesion Science & Technology* 17 (4), 519–546.